Chapter 6

Growth and Photovoltaic behavior of (1-x)$KNbO_3$-x$Ba(Ni_{1/2}Nb_{1/2})O_{3-\delta}$ Thin Films and Application of ZnO nano-structures as light trapping layer in device

6.1 Introduction:

In Recent years, solar cells have become more attractive for carbon emission-free energy technology to meet the goals of environmental protection. Promising results with high efficiency in solar cells based on organometallic-halides with perovskite structure have motivated to study the photovoltaic phenomena in oxide perovskite materials also [P. Gao et al. (2014)]. Recently, Ni and Nb-doped $KNbO_3$ have been widely investigated because of their high spontaneous polarization and promising applications as solar energy harvesting material [I. Grinberg et al. (2013)]. Band gap tuning of $KNbO_3$ produced a semiconducting solid solution $[KNbO_3]_{1-x}$-$[Ba(Ni_{0.5}Nb_{0.5})O_{3-\delta}]_x$ (KNBNN) having a lower band gap of 1.1 eV without losing the ferroelectricity [W. Zhou et al. (2014)]. KNBNN is a multiferroic material with a large electrical polarization and weak ferromagnetism at room temperatures [W. Zhou et al. (2014)]. Even though the KNBNN have lower band gap around 1.1 eV, but, very low device efficiency is reported for its bulk photovoltaic effect [I. Grinberg et al. (2013)]. Synthesis of $KNbO_3$ thin film by pulsed laser deposition and magnetron sputtering has delineated and provide a way to use it for solar-energy device applications [I. T. Weber et al. (2005); T. H. Lee et al (2016)]. But there is no report on magnetron sputtered KNBNN thin film based photovoltaic studies. Unlike silicon and organic thin films solar cells, ferroelectric-photovoltaic thin film solar cells showed low short-circuit photocurrent. Lower photocurrent in thin film ferroelectric solar cells may be due to wide band gap of ferroelectrics e.g., ~2.4 eV for BFO and PZT [B. Chen et al. (2011); Z. Tang et al. (2014)]. Another reason for lower photocurrent in thin film solar cells is absorption reduction in photoactive layer due to nanometre thin films. Various theoretical studies have indicated that use of nanostructured materials could improve thin film photovoltaic device efficiency due to their extremely high surface to volume ratio [A. Campa et al. (2010)]. Variously engineered nanostructures are integrated into the thin films solar cells to increase the absorption in photoactive layer by trapping the light within the surface [H. A. Atwater et al. (2010); C. F. Bohren et al. (2008)]. The trapping of light inside device is possible by increasing the optical path length of incident photons. Anti-reflecting structures such as textured electrode, dielectric gratings, photonic crystals, nanorods, nanotips and pyramidical structures were used to increase the optical path length by scattering the incident light in its randomly oriented surface [H. Zhou et al. (2014); M. A. Green et al (2012); P. Ravirajan et al (2006); S. F. Leung et al. (2014); J. Zhu et al. (2009); V. Bhavnasi et al. (2013); J. Zhu et al. (2010)].

Semiconducting nanostructures have been developed and explored for the variety of electronic devices. The ordered assembly of three-dimensional nanostructures have unique intrinsic properties, and when they coupled with an active layer of photovoltaic devices, precise tuning of the physical properties of heterostructures reported [S. F. Leung et al. (2014); S. H. Lim et al. (2007)]. The properties of heterostructures are directly influenced by shape, size, surface area, surface roughness, alignment and density of integrated nanostructures. Among all electron transport oxide semiconducting materials, Zinc oxide (ZnO) is widely used because of its high transparency, excellent electrical properties and feasibility to form great variety of nano-morphologies (quantum dots, nanoparticles, nanorods, nanowalls, nanosheets, nanotips, nanoflowers and branched nanorods) by low-cost and straightforward synthesis process [J. Qiu et al. (2011); C. Y. Jiang et al. (2007); M. Guo et al. (2004); J. Theerthagiri et al. (2019)]. ZnO with wide band gap (3.37 eV) have higher electron mobility, is reported to exhibit appreciable results in electronic devices [D. C. Look (2001)]. Zinc oxide (ZnO) is a semiconductor which is thermally and chemically stable. ZnO nanostructured materials are studied mainly as promising light trapping materials to improve photovoltaic device efficiency as well as production cost reduction [V. Consonni et al. (2019)]. The nanostructured ZnO can be utilized as light trapping layer and also continuous conductive pathways for photo-generated carriers transport to minimize the carrier recombination [Y. J. Lee et al. (2008)]. Indeed, multiple studies have already shown the potential application of nanostructured ZnO as the functional element for sensors, photo-diodes, transistors, and light-emitting diodes, but, their light scattering properties still require in-depth study [V. Consonni et al. (2019); P. P. Das et al. (2014)].

In the present work, various compositions of ceramic solid solution $(1-x)KNbO_3-xBa(Ni_{1/2}Nb_{1/2})O_{3-\delta}$ (KNBNN) were synthesized by solid state reaction method. Afterwards, we have successfully prepared the KN-BNN thin films by magnetron sputtering and chemical solution deposition technique and investigated its application as photovoltaic active layer. We have synthesized ZnO nanoparticles, nanorods and nanowalls also by chemical solution technique, and studied their growth mechanism and optical properties. Chemical solution deposition techniques are used because it's easy, cost-effective and provide certain degrees of freedom in optimizing the physical properties of the material by controlling the surface morphology of films. We have investigated the structural and light scattering properties of ZnO nanoparticles, nanorods, nanowalls and their effect on photo-response of KN-BNN thin film based photovoltaic devices. We report a direct and detailed analysis of the effect of ZnO nanostructures incorporation on optical and electrical properties at nanoscale.

6.2. Experimental Details

The ceramic solid solutions of (1-x)$KNbO_3$-xBa($Ni_{1/2}Nb_{1/2}$)$O_{3-\delta}$ (KNBNN) with compositions x = 0.05, 0.10,0.15, 0.20, and 0.25 were synthesized by solid state reaction method. The raw materials were K_2CO_3, Nb_2O_5, $BaCO_3$, and NiO which were all in the analytical reagent grade with more than 99% purity. According to the particular composition of KNBNN solid solution, stoichiometric starting reagents were hand-mixed by using an agate mortar and pestle. After premixing, all constituent oxide powders were ball milled in acetone medium for 6 hours. The ball milled reactant powder of KNBNN were dried and calcined at 800°C in air atmosphere for 5 hours to form desired KNBNN ferroelectric perovskite phase. Circular pellets of calcined powder were prepared by hydraulic pressing using water solution of PVA as binder. The green pellets were sintered in closed sintering chamber and sintering temperature was optimized to get highly dense pellets. The two-inch diameter ceramic target of 0.90KNBNN composition was prepared by pressing the calcined powder. The green pellet was sintered at 1050°C for an hour to form KNBNN ceramic target. It has been difficult to grow stoichiometric 0.90KNBNN thin film due to low evaporation temperature of K_2O during growth. In order to maintain the stoichiometric ratio of elements in 0.90KNBNN thin film, the compensatory K-excess target was prepared and closed sintering K_2O environment was used during process.

The phase purity of the KNBNN solid solution was analyzed by RIGAKU X-ray diffractometer (MINIFLEX 600) with Cu-Kα radiations. The morphologies and particle size of KNBNN solid solutions were obtained by high-resolution scanning electron microscope (ZEISS, Evo Research18) and elemental analysis was investigated with X-Ray energy-dispersive spectrometer (EDS) equipped with HR-SEM. The UV-visible absorbance spectra of calcined KNBNN powder samples were recorded using

Spectrophotometer (UV-1800, SHIMADZO). The optical band gap was calculated from absorption data using Tauc's equation. For electrical polarization measurements, the sintered pellets were polished and Ag paste was applied on both flat sides of the pellets which act as electrodes. The dielectric permittivity, dielectric-loss and resistive behavior were measured at various frequencies with changing the temperature using Keysight-E4990A impedance analyzer. The ferroelectric polarization as a function of external electric field was examined by Precision Premier -II ferroelectric tester based on standard Sawyer-Tower circuit (Radiant Technologies) in frequency range from 1 to 1000 Hz at room temperature.

In order to investigate the surface topography and electrical properties of KNBNN, thin films were deposited on FTO coated glass substrates by sputtering. The surface potential distribution and resistive switching behavior were measured using KPFM. The AFM, PFM and KPFM measurements were performed at room temperature using scanning probe microscope (NT-MDT) with a platinum coated Si cantilever. The current –voltage characteristics were measured using Pt tip as top electrode and FTO as bottom electrode. The current-voltage curves were recorded by performing forward and reverse voltage scans between -10 V and +10V at a scan rate of 100 mV/s. The electrical properties of samples were measured using current-sensing atomic force microscopy (C-AFM) mode under precisely controlled load force between tip and the samples. The white source light and 532 nm laser (hν = 2.33 eV) was used as light source to measure the photovoltaic properties. The current–voltage (I-V) measurement and transient photo-response of as prepared device were measured using Keithley 2400 source- meter interfaced with a computer.

6.3. Results and Discussion

6.3.1 Room Temperature Structural characterization

The x-ray diffraction (XRD) patterns of $0.90KNbO_3$-$0.10Ba(Ni_{1/2}Nb_{1/2})O_{3-\delta}$ (0.9KNBNN) ceramic sintered at various temperatures in the range 990°C to 1125°C are depicted in the Fig.6.1. With increasing the sintering temperature from 990°C to 1050°C, the density increased from 3.4 g/cm^2 to 4.6 g/cm^2 while impurities present at lower sintering temperatures got removed. Further increase in sintering temperature enhanced the density but new impurity phases appeared again. The impurities appear because of the presence of volatile potassium which starts evaporating above 800°C and lead to excess amount of Ni^{2+} and Nb^{5+} at higher sintering temperature and deviation from stoichiometry. The powder XRD pattern of $0.90KNbO_3$-$0.10Ba(Ni_{1/2}Nb_{1/2})O_{3-\delta}$ can be indexed using orthorhombic crystal structure similar to the pure perovskite phase of $KNbO_3$ [JCPDF No. 32-0822]. The XRD pattern and crystal structure of 0.9KNBNN solid solution shows good consistency with earlier reported work [I. Grinberg et al. (2013)].

Fig 6.2 shows the XRD patterns of the KNBNN solid solution for x = 0.05 to 0.25. For the composition with x = 0.05 and 0.10, the Bragg reflections can be easily indexed to the orthorhombic crystal system of the Amm2 space group, similar to that for pure $KNbO_3$. With further doping of BNN in $KNbO_3$, the peak splitting for pseudocubic (001) profile is reduced whereas the (110) pseudocubic peak shows slightly enhanced splitting. This suggests that the lattice distortion is getting modified with the solid solution formation; however, the structure remains the orthorhombic. Similar results were earlier reported for this solid solution system [C. Li et al. (2018)].

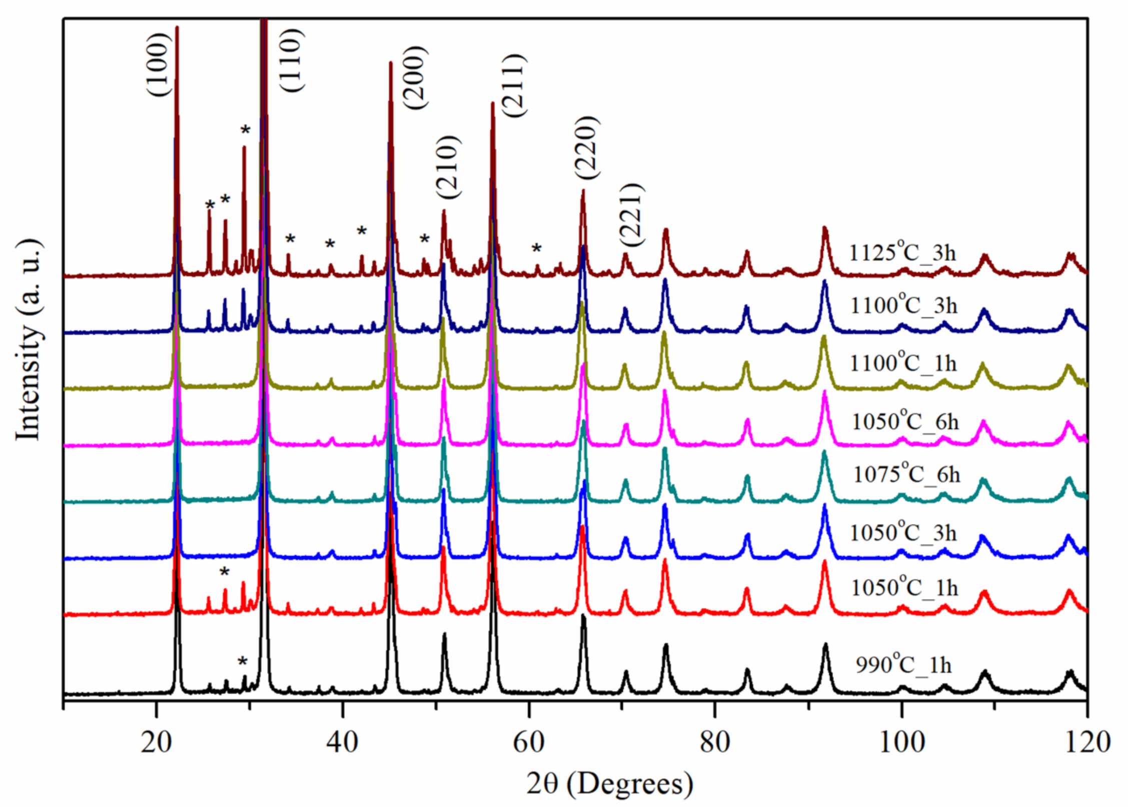

FIGURE 6.1 X-Ray Diffraction patterns of $0.90KNbO_3$-$0.10Ba(Ni_{1/2}Nb_{1/2})O_{3-\delta}$ solid solutions sintered at 990 °C to 1125°C. The impurities are marked with * sign.

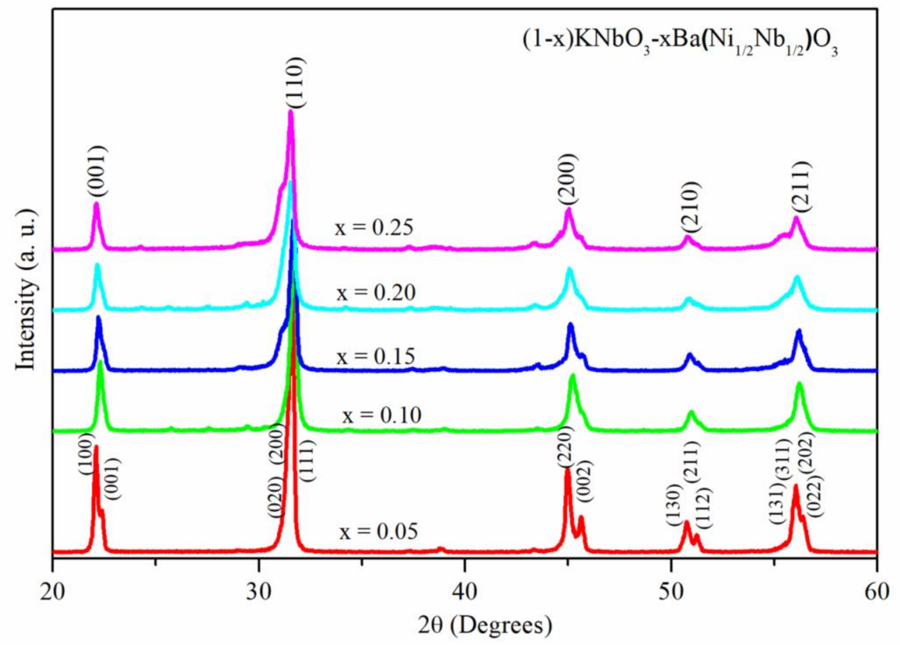

FIGURE 6.2 X-ray diffraction patterns of $(1-x)KNbO_3$-$xBa(Ni_{1/2}Nb_{1/2})O_{3-\delta}$ ceramic solid solutions with compositions of (x = 0.05, 0.10,0.15, 0.20, 0.25).

6.3.2 Optical Band gap analysis

Fig. 6.3 shows the UV-visible absorption spectra of as prepared KNBNN ceramics in the wavelength rang of 380-1100 nm. In visible region, the absorption starts increasing around $\lambda = 600$ nm. The absorption spectra show a major peak (A1) in ultraviolet region and A2, A3, A4 peaks are in visible region. Peak (A2) at $\lambda = 430$ nm (~2.88 eV) is clearly visible for BNN doped compositions while it's absent for pure $KNbO_3$ sample. Absorption peak at $\lambda = 430$ nm wavelength overlaps with the edge of the intrinsic band gap absorption. The second peak centers at $\lambda = 715$ nm (~ 1.73eV) which has two minor shoulder A2 and A4 at $\lambda = 645$ nm and $\lambda = 803$ nm respectively. The fifth peak A5 is observed at $\lambda = 1092$ nm (1.13 eV) which falls in infrared region. The absorption peak in NIR region may be attributed to oxygen vacancies due to Ni^{2+} doping. The absorption peak A1 is due to $KNbO_3$ intrinsic absorption process and it is due to $^3A_{2g}(^3F)$ to $^3T_{1g}(^3P)$ transition. Absorption peaks A3 and A4 lie in KNBNN intrinsic absorption area and are due to Ni^{2+} doping. The observed peaks A3 and A4 can be attributed to $^3A_{2g}(^3F)$ to $^3T_{1g}(^3F)$ transition. The A2 peak is due to the $^3A_{2g}(^3F)$ to $^1E_{1g}(^3D)$ transition. The infrared peak A5 at $\lambda = 1092$ nm could be assigned to the $^3A_{2g}(^3F)$ to $^3T_{2g}(^3F)$ transition [P. Wu et al. (2016); S. L. Reddy et al. (2012); M. Triest et al. (2000)].

The optical band gap of KNBNN samples were calculated using 'Tauc' equation $(\alpha h\nu)^2 = \beta(h\nu - E_g)$ where 'α' is the absorption coefficient, 'β' is a constant, 'E_g' is energy band gap, 'ν' is the frequency of photon and 'h' is the Planck's constant. Fig. 6.4 shows the Tauc plot for the optical band gap of KNBNN ceramics. From the extrapolation of the linear part of the slop of $(\alpha h\nu)^2$ vs. E_g to the x-axis (E_g), the band gap of KNBNN is evaluated. There are two linear region found on $(\alpha h\nu)^2$ vs E_g plot, which provide two different band gaps for KNBNN samples. These results are consistent with First

Principle calculations results reported earlier [I. Grinberg et al. (2013)] which gives two direct band gap E_{g1} ~1.84 eV and E_{g2} ~ 1.49 eV, for 0.33$KNbO_3$-xBa$(Ni_{1/2}Nb_{1/2})O_{3-\delta}$ composition.

The band gap (E_{g1}) for KNBNN compositions x = 0.0, 0.05, 0.1, 0.15, 0.20, and 0.25 are 3.1 eV, 2.40 eV, 2.21 eV, 2.19 eV, 2.29 eV, and 2.39 eV respectively. Undoped $KNbO_3$ shows no extra absorption peak in its visible region so it has only one (E_{g1}~ 3.1eV) band gap. With BNN doping, the band gap decreases from 3.1 eV to 2.40 eV for 0.95KNBNN composition and it has also a second band gap E_{g2} = 0.96 eV. With further increasing the BNN concentration, the band gap reduced to 2.19 eV for x=0.15 and it start increasing on further increasing the BNN concentration as shown in Fig 6.4. The evolution of second band gap E_{g2} for all these compositions of KNBNN are shown in Fig. 6.5 and it is observed that E_{g2} is lower than 1.14 eV. The band gaps for 0.9KNBNN Sample is estimated to be E_{g1} ~ 2.21 eV and E_{g2}~ 1.0 eV, which is in agreement with earlier reported band gap of KNBNN ceramics [C. Li et al. (2018); I. Greenberg et al. (2013)]. The tauc plot and estimation of band gap E_{g1} and E_{g2} for 0.9KNBNN are shown in Fig. 6.6.

A possible theoretical explanation for change in the band gap of KNBNN ceramics can be given by the band structure model illustrated in Fig 6.7. $KNbO_3$ is a ABO_3 type ferroelectric perovskite oxide. The lowest energy band, i.e., Valence band maximum (V.B.) of $KNbO_3$ is composed of mainly O-2p orbitals states while the conduction band minimum (C.B.) is mainly constituted by Nb-4d states [T. Su et al. (2010)]. The energy difference between top of the O-2p (valence band maximum) and bottom of the Nb-4d (conduction band minimum) provides the band gap value of $KNbO_3$ as shown in Fig. 6.7 (a). The charge transfer transitions from V.B. to C.B., experimentally provides the band gap and it is reported that $KNbO_3$ has wide band gap (3.3 eV) for cubic phase. In our samples, we found lower band gap ~ 3.1 eV for $KNbO_3$ which may be due to orthorhombic ferroelectric distortion and presence of few oxygen vacancy states as shown in Fig. 6.7(b). The samples with BNN doping, the V.B. will be formed by hybridization of Ni-3d and O-2p states and conduction band minimum will be composed by Nb-4d and Ni-3d states as shown in Fig. 6.7 (c).

For KNBNN ceramic, the acceptor band due to Ni^{2+} is located at the top of the valence band and defect induced new energy bands due to oxygen vacancies are located below the conduction band as shown in Fig 6.7 (c). It is earlier reported that sub-band due to oxygen vacancies locates below C.B. [A. J. Hauser et al. (2008)]. With BNN doping in $KNbO_3$, band gap has red-shifts and reduced to E_{g1} ~2.19 eV and E_{g2} ~1.0 eV for x=0.15. The reduced band gap in KNBNN is due to filled Ni-3d gap states between C.B. and V.B. states. There will be hybridized Ni-3d and O-2p states near V.B. and another hybridized state will occur below C.B. The band-to-band transition between Ni-3d hybridized state give the E_{g2} band gap which is lower than E_{g1} band gap as shown in Fig. 6.7 (e). The band gap in NIR region is due to presence of oxygen vacancies in KNBNN samples. After BNN doping in $KNbO_3$ lattice, two possible configurations for oxygen vacancies are expected, Ni-V_o-Ni and Ni-V_o-Nb. According to theoretical study, it is reported that Ni-V_o-Nb configuration shows lower band gap and it is more dominant at low doping percentage [I. Grinberg et al. (2013)]. The presence of oxygen vacancies creates new energy states bellow the conduction band and thus, it is reported that oxygen vacancies can lower the band gap by ~ 0.5 eV [T. T. Qi et al. (2011)]. In some cases, it is reported that oxygen vacancies act as recombination centers and are detrimental to polarization switching [F. G. Wang et al. (2014)] while in some cases, it is reported that new energy states created due oxygen vacancies act as charge transfer states and prevent the charge recombination and increase the charge transportation process [I. Nakamura et al. (2000)]. Thus, low band gap KNBNN ceramics can be very useful as photoactive material for photovoltaic devices and also have potential application in NIR-related devices.

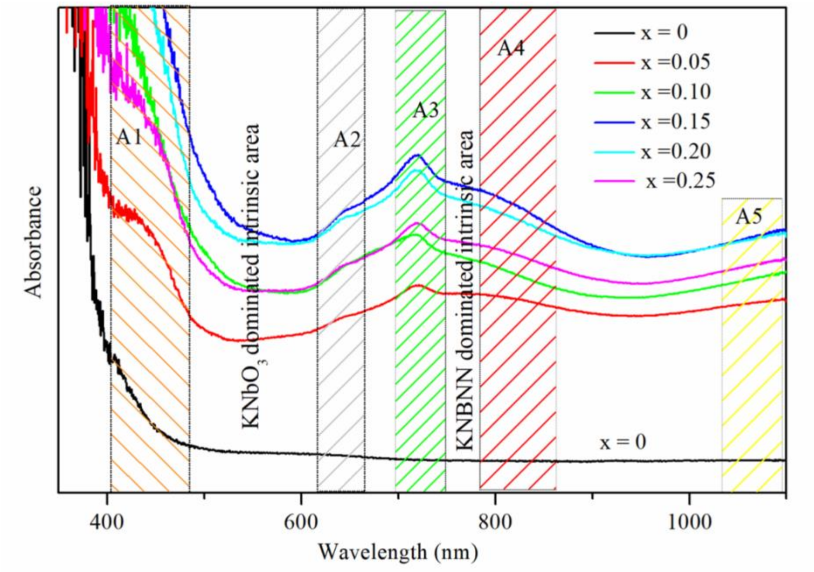

FIGURE 6.3 Variation of absorption spectra of (1-x)$KNbO_3$-(x)$Ba(Ni_{1/2}Nb_{1/2})O_{3-\delta}$ solid solution for various compositions in the range ($0.0 \leq x \leq 0.25$).

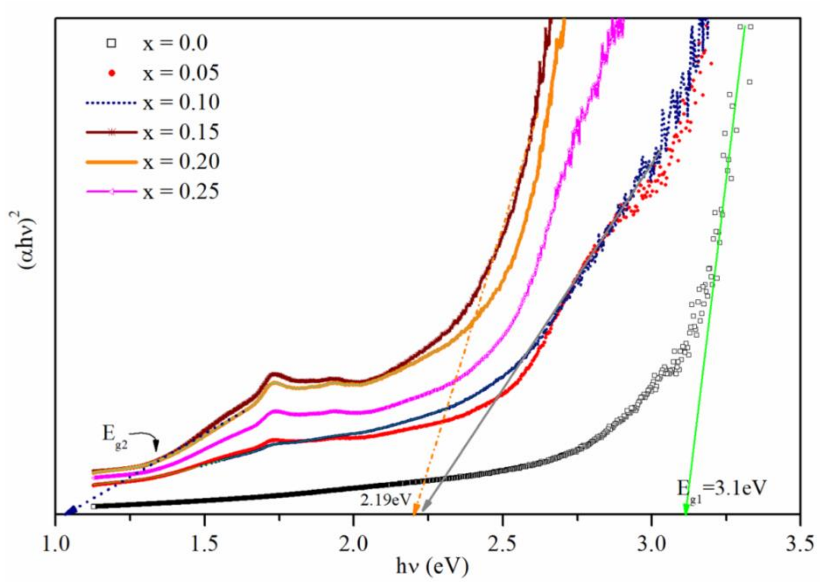

FIGURE 6.4 Optical band gap of (1-x)$KNbO_3$-(x)$Ba(Ni_{1/2}Nb_{1/2})O_{3-\delta}$ solid solution for various compositions in the range ($0.0 \leq x \leq 0.25$). Extrapolated intercept is not shown for all compositions for better clarity of the figure.

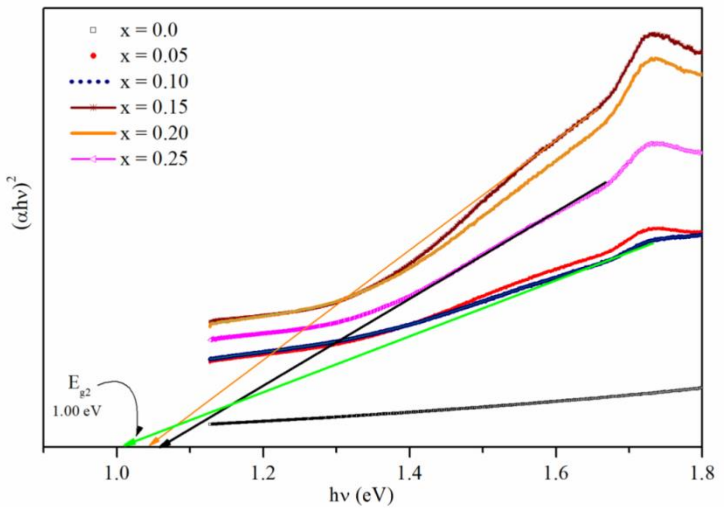

FIGURE 6.5 Direct band gap (E_{g2}) of (1-x)$KNbO_3$-(x)$Ba(Ni_{1/2}Nb_{1/2})O_{3-\delta}$ solid solution for various compositions in the range ($0.0 \leq x \leq 0.25$). Extrapolated intercept is shown for three compositions only for better clarity of the figure.

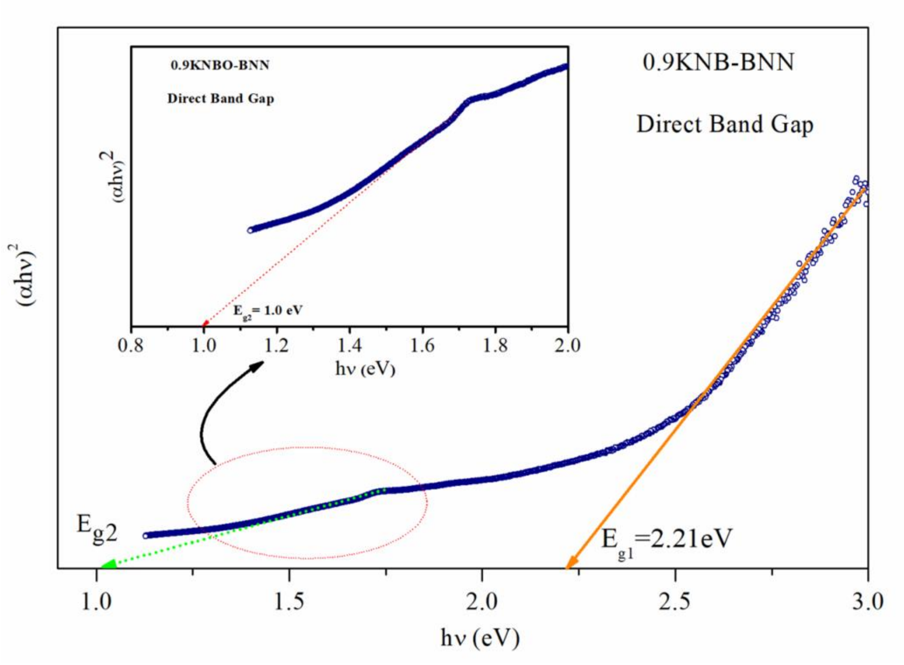

FIGURE 6.6 Band gaps for 0.9$KNbO_3$-(0.10)$Ba(Ni_{1/2}Nb_{1/2})O_{3-\delta}$ solid solution. Inset is showing direct band gap (E_{g2}).

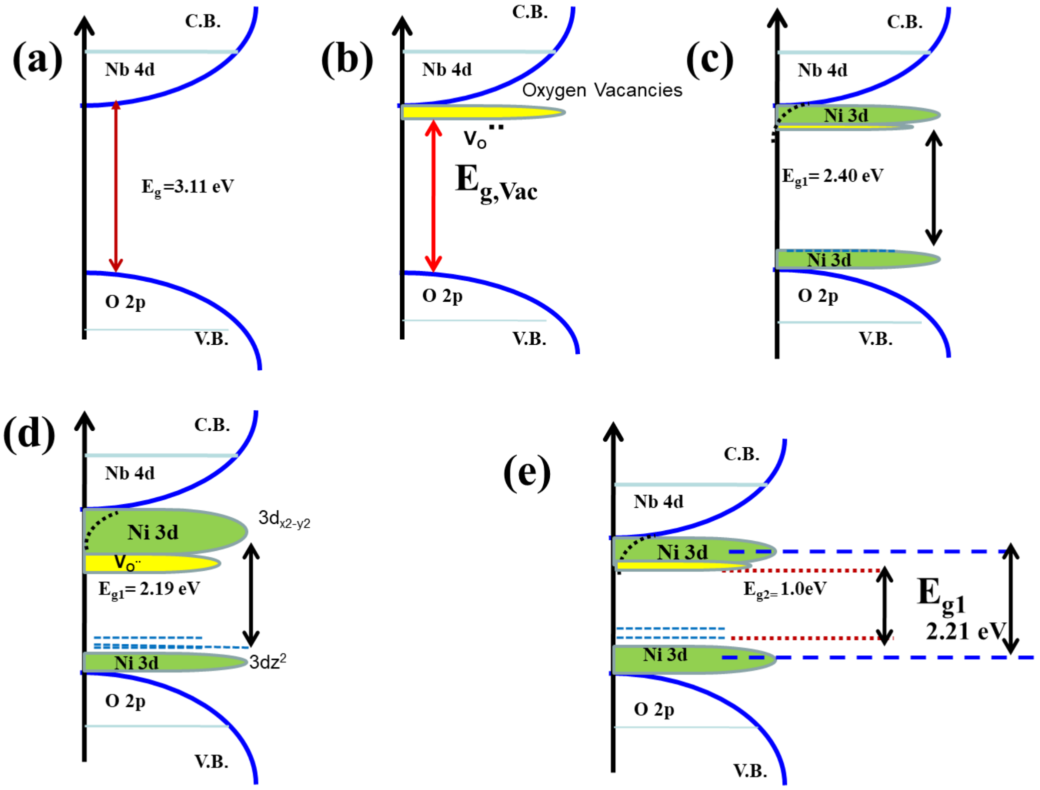

FIGURE 6.7 Schematic diagrams of density of electronic states (a) Ideal Situation for $KNbO_3$ (b) With presence of oxygen vacancies in $KNbO_3$ (c) with effect of Ni^{2+} 3d states for KNBNN (d) higher doping percentage of BNN in KNBNN and (e) E_{g1} and E_{g2} band gap in 0.90KNBNN composition.

6.3.3 Raman studies and Dielectric properties of $0.90KNbO_3$-$0.10Ba(Ni_{1/2}Nb_{1/2})O_{3-\delta}$ Ceramic

Raman spectroscopy is a non-destructive technique to find out the structure and phase transition in materials. In order to know the signature of ferroelectricity in $0.90KNbO_3$-$0.10Ba(Ni_{1/2}Nb_{1/2})O_{3-\delta}$ (0.9KNBNN) solid solution, we performed Raman scattering analysis. Fig. 6.8 (a) shows the Raman spectra of 0.9KNBNN sample. The modes assignments of 0.9KNBNN are done according to the earlier reported literature [C. Li et al. (2018)]. As shown in Fig 6.8 (a), a broad $A_1(TO_1)$ mode is observed at 270 cm^{-1} which is due to BO_6 bending vibrations. Due to broadening of $A_1(TO_1)$ mode, few possible peaks which are not clearly visible should be at 233 cm^{-1} and 290 cm^{-1} . These are assigned to mode $(B_1)(TO_1)$ and $A_1(TO_4, LO_4)$ respectively. A weak mode $(B_1, B_2)(TO_2)$ is centered at 193 cm^{-1}. These modes confirm the presence of long-range polar order in 0.9KNBNN crystal structure. One new peak is found at 112 cm^{-1} and assigned as 'N' means new mode which is due to BNN doping. The $B_2(TO_3)$ mode (at 534 cm^{-1}), $A_1(TO_3)$ mode (at 597 cm^{-1}) are associated with vibrations of the octahedral. The presence a resonance depth at 200 cm^{-1} and $(B_1+B_2+A_1(LO_3))$ mode at 832 cm^{-1} confirm the ferroelectricity in 0.9KNBNN.

Fig. 6.8 (b) shows the temperature dependent dielectric permittivity of 0.9KNBNN composition. The dielectric permittivity starts increasing at 240°C and a clear ferroelectric to paraelectric transition is observed with T_c at 402°C. The ferroelectric phase of 0.9KNBNN starts to weaken from 240°C and complete ferroelectric to paraelectric cubic phase transition occurs at 402°C. The dielectric loss increases with increasing temperature as shown in inset of Fig. 6.8(b).

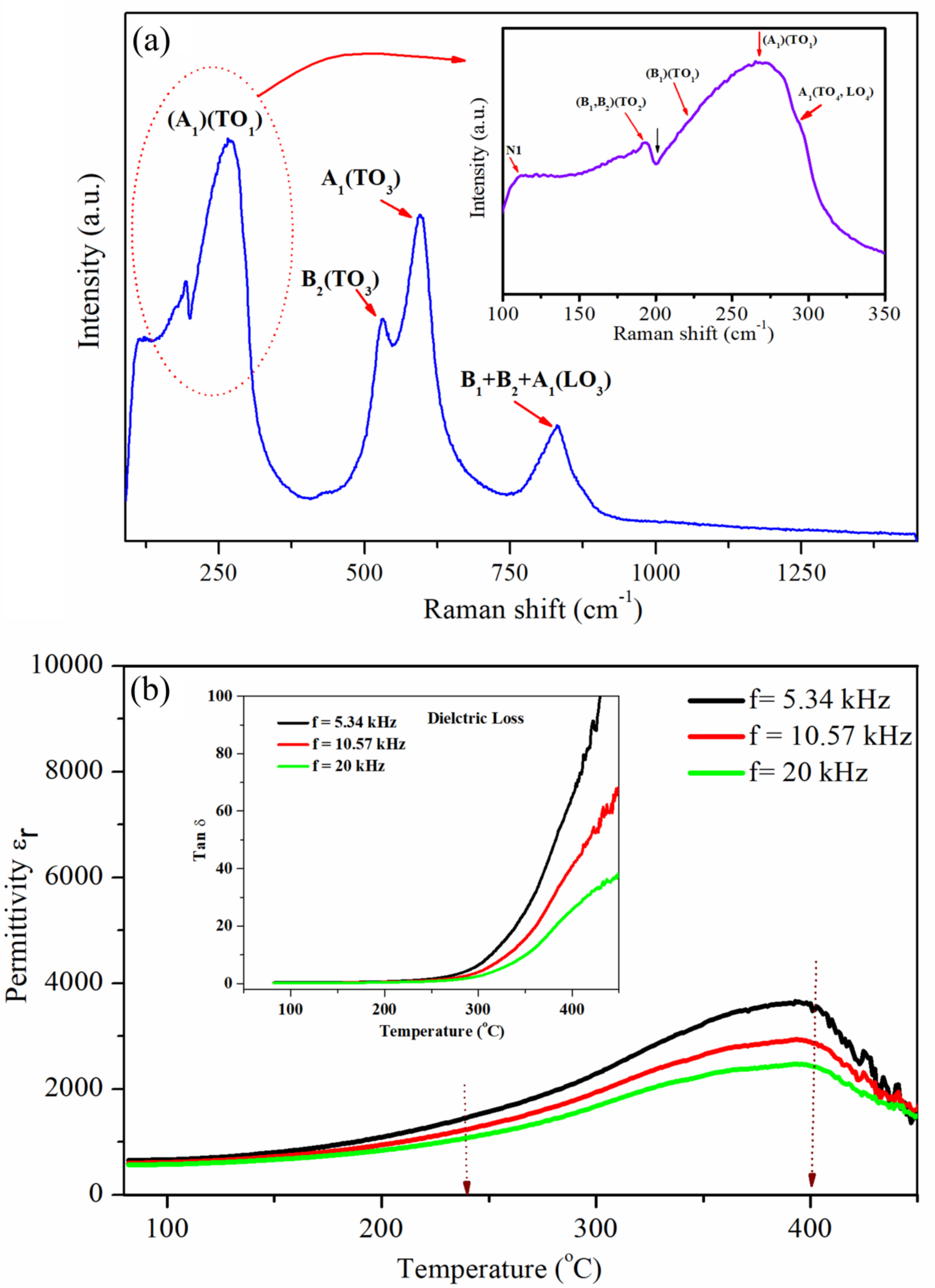

FIGURE 6.8 (a) Raman scattering spectra for the 0.90KNBNN sample. Inset shows the enlarged view of lower range Raman shift data (100-350 cm^{-1}). (b) Temperature dependent relative permittivity of 0.9KNBNN sample. Inset is showing the temperature dependent dielectric loss.

6.3.4 Synthesis of 0.90KNbO$_3$-0.10Ba(Ni$_{1/2}$Nb$_{1/2}$)O$_{3-\delta}$ thin films by magnetron sputtering

Since the composition 0.90KNbO$_3$-0.10Ba(Ni$_{1/2}$Nb$_{1/2}$)O$_{3-\delta}$ has optimally reduced band gap, we selected this composition for further investigations. Three types of substrates, FTO coated glass, silicon wafer and quartz were used for depositing thin films of 0.9KNBNN target by RF magnetron sputtering. Prior to deposition, the chamber was evacuated to 10^{-6} mbar by using vacuum pump. The oxygen pressure was kept 200 mTorr during deposition and the substrate temperature was around 650°C. After deposition, films were annealed for an hour at 650°C under oxygen and argon atmosphere. All deposition parameters are given in Table 6.1. For synthesis of KNBNN thin films, all precautions were taken as suggested by Lee et al [T. H. Lee et al. (2016)]. Schematic drawing of 0.9KNBNN thin film deposition configuration using magnetron sputtering and sputtering process is shown in Fig 6.9 (a). The ions created by gas discharge strike on the target and release the KNBNN molecules. The target acts as cathode and substrate holder as anode so that the KNBNN molecules are deposited on substrates. Device configuration using FTO and silicon substrates are shown in Fig 6.9 (c) and (d).

Table 6.1 Deposition parameters for 0.9KNBNN thin films by Magnetron Sputtering

Material	**0.9KNBNN**
Target Diameter	2 inches
Power	50-100 W
Time	2h-4h
Substrate Temperature	650 °C
Partial pressure of (Ar+O$_2$)	200 mTorr

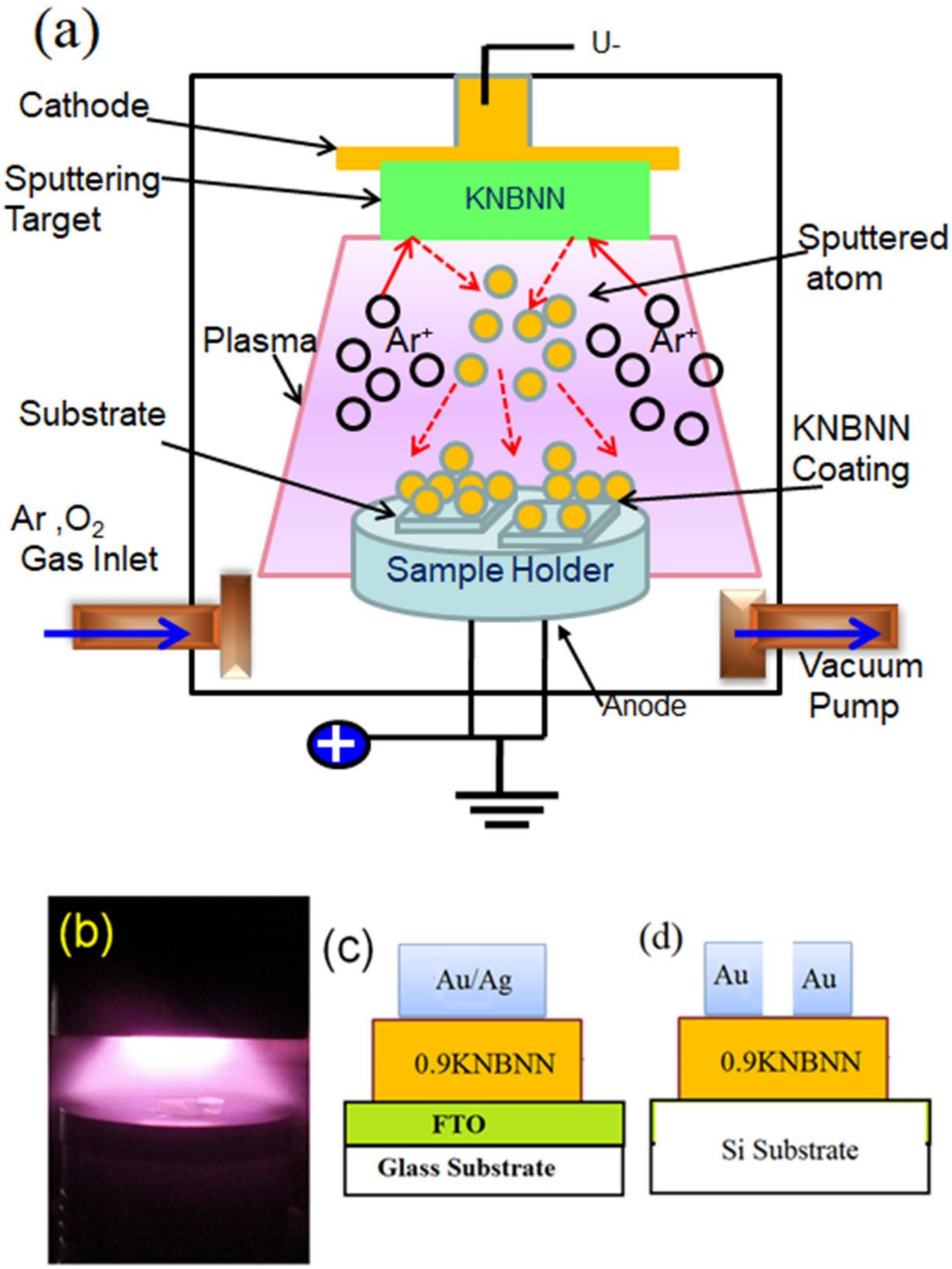

FIGURE 6.9 Schematic drawings of 0.9KNBNN thin film deposition configuration using magnetron sputtering (a) Sputtering process (b) Image of running sputtering process showing the plasma formation (c) Device configuration using FTO substrate and (d) KNBNN film deposited on silicon wafer with parallel electrode.

6.3.5 XRD, HRSEM and optical band gap analysis of 0.9KNBNN films

The crystallographic phase present in the KNBNN thin films were analyzed using XRD. Fig. 6.10 (a) and (b) show the XRD patterns of KNBNN thin films deposited on quartz and FTO substrates respectively. The desired KNBNN perovskite phase is retained in the film. The films showed crystallization along the (110) direction of KNBNN. The pseudo-cubic indices of the peaks at $2\theta = 22.1°$ to (100), 31.6° to (110), and 45.6° to (200) are in good agreement with 0.9KNBNN perovskite solid solution as shown in Fig 6.1. Due to the lower intensity of the XRD peaks, peak splitting for orthorhombic phase is not seen clearly. The XRD patterns indicate that the films formed on quartz and FTO substrates are well crystallized. It is confirmed that no other peak is observed in KNBNN films deposited on quartz substrate while extra FTO substrate peaks (at $2\theta = 24°$, 26.6°, 34° and 37°) are observed in 0.9KNBNN films deposited on FTO. The HRSEM image of cross section 0.9KNBNN/FTO is shown in Fig 6.11 (a). The thickness of 0.9KNBNN is around 370 nm which is also confirmed by thickness profilometer. The HR-SEM image of surface of 0.9KNBNN is shown in Fig. 6.11 (b) which confirms its polycrystalline nature. The films are densely packed and no pores are observed.

As shown in Fig. 6.12 (a), the optical absorption spectra of 0.9KNBNN has two major absorbance peaks A1 in UV region and A2 in visible range. The direct band gap of thin film is measured using Tauc's plot and two band gaps Eg1~ 2.05 eV and Eg2~ 1.63 eV are obtained. Inset of Fig. 6.12 (a) is showing the schematic presentation of intraband electronic transition in the material. The Eg1~ 2.05 eV band gap can originated due to band-to-band transition from V.B. (hybridized Ni-3d and O-2p) to C.B. (Nb-4d states).The Eg2~ 1.63 eV band gap can be due intraband transition of Ni-3d orbitals (from $d_z{}^2$ to $d_x{}^2\text{-}_y{}^2$orbital).

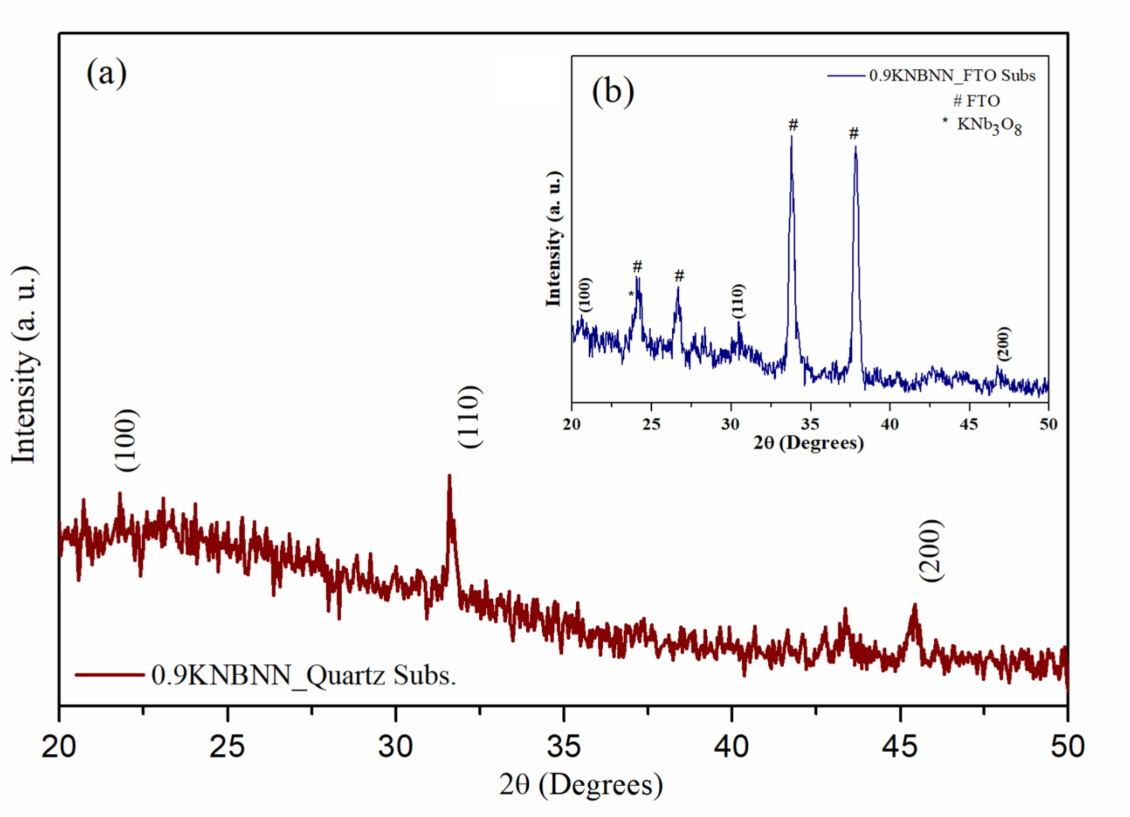

FIGURE 6.10 (a) XRD patterns of magnetron sputtered 0.9KNBNN thin films grown on (a) quartz substrate and (b) on FTO coated glass substrate shown in inset.

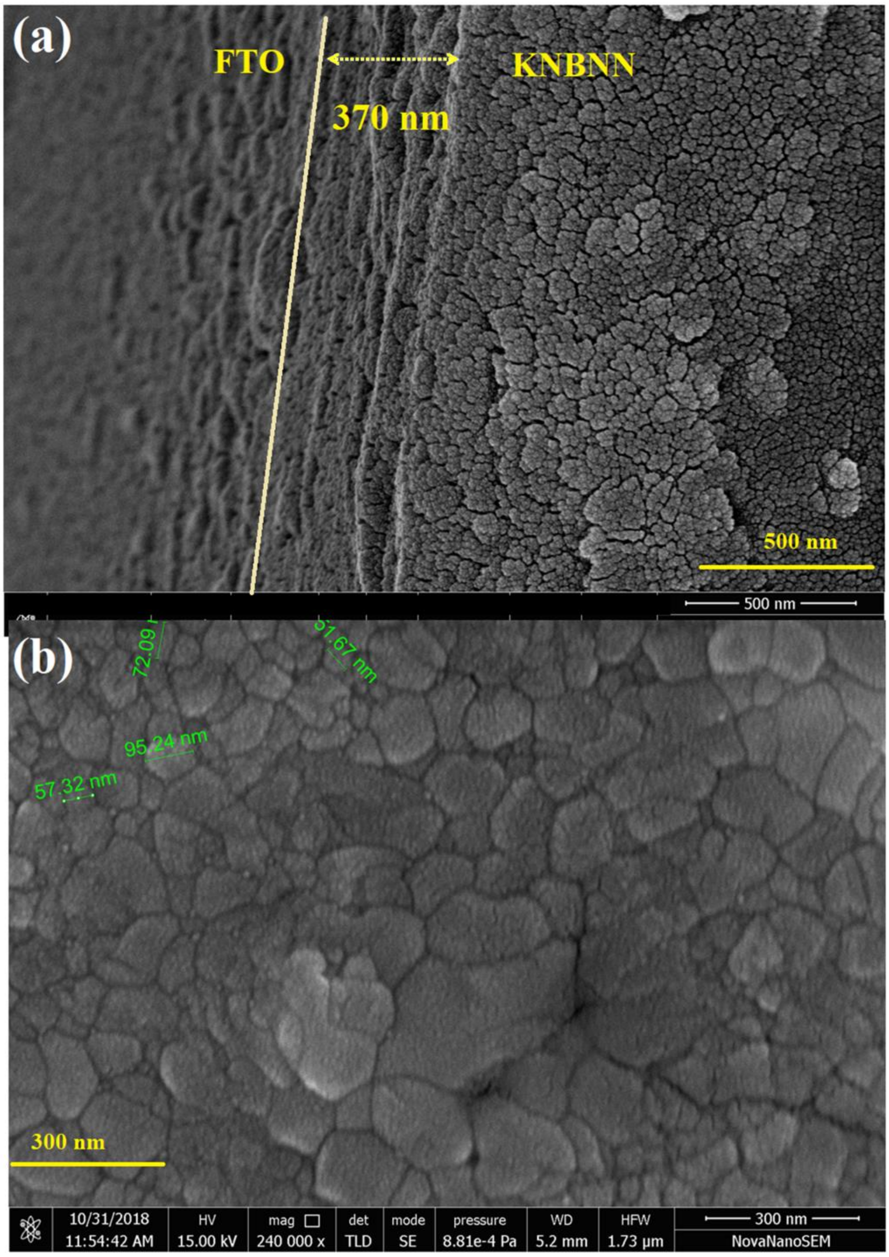

FIGURE 6.11 (a) Cross-section HRSEM image of 0.9KNBNN thin film deposited on FTO coated Glass substrate and (b) HRSEM image of magnetron sputtered 0.9KNBNN thin film surface.

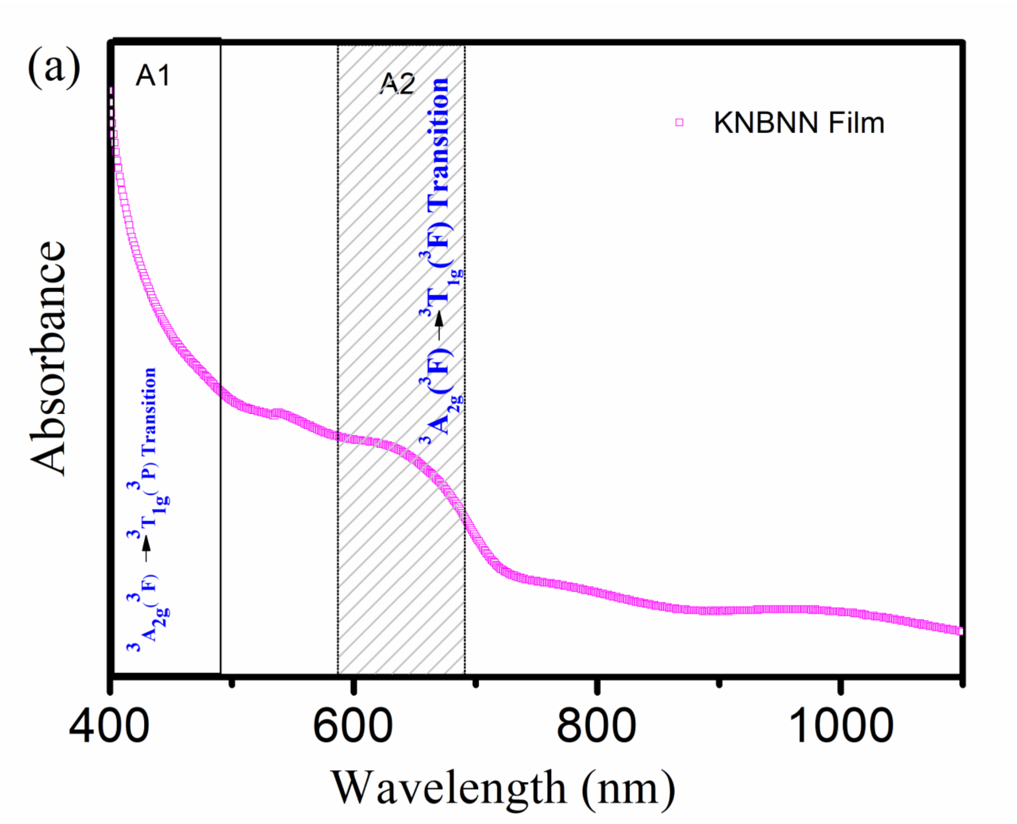

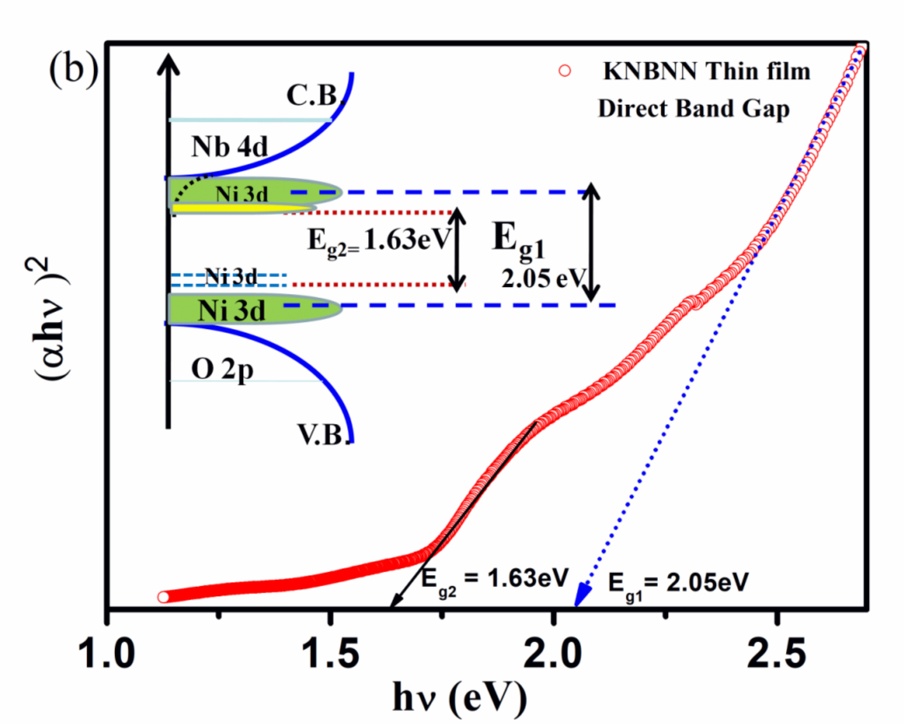

FIGURE 6.12 (a) UV-visible absorption spectra of magnetron sputtered 0.9KNBNN thin films and (b) Tauc plot for absorption spectra showing direct band gap. Inset is showing the schematic presentation of intraband electronic transition in material.

6.3.6 Atomic force and Piezo-force microscopy Analysis

The morphological characterization of the magnetron sputtered 0.9KNBNN thin films were done using atomic force (AFM) and Piezo-force microscopy (PFM). The AFM topography and local ferroelectric behavior of 0.9KNBNN thin films were probed by piezoresponse force microscopy. The AFM Topography images of magnetron sputtered 0.9KNBNN thin films deposited on FTO coated glass substrate, at 50W, 100W and (50W+100W) rf-power are shown in Fig. 6.13 (a), (d), (g) and their respective roughness profiles are shown in Fig. 6.13 (b) (e), (h). For the 0.9KNBNN thin film deposited at 50W, the average roughness is estimated around 14 nm while the film deposited at 100 W shows very high roughness around 31 nm. The topography image shows that film deposited at 50W rf power have some distinct features due to low deposition rate. Film surface shows dense granular structure with small elongated grains.

As can be clearly observed from Fig. 6.13 (d), (g), the films deposited at high sputtering powers have high roughness. The film surface consists of almost circular grain but an accumulation of grains is also observed which causes the higher roughness of film. Figs. 6.13 (c), (f) and (i) illustrate the AFM topography view in 3-D. As can be seen in Fig. 6.13 (g), the film deposited in two steps (50W+100W) rf power also shows high roughness. The film was first grown at slow deposition rate (50W power) and then power increased to 100 W. The film has rms roughness around 36 nm but accumulation of grains is reduced and a film looks more crystalline in nature.

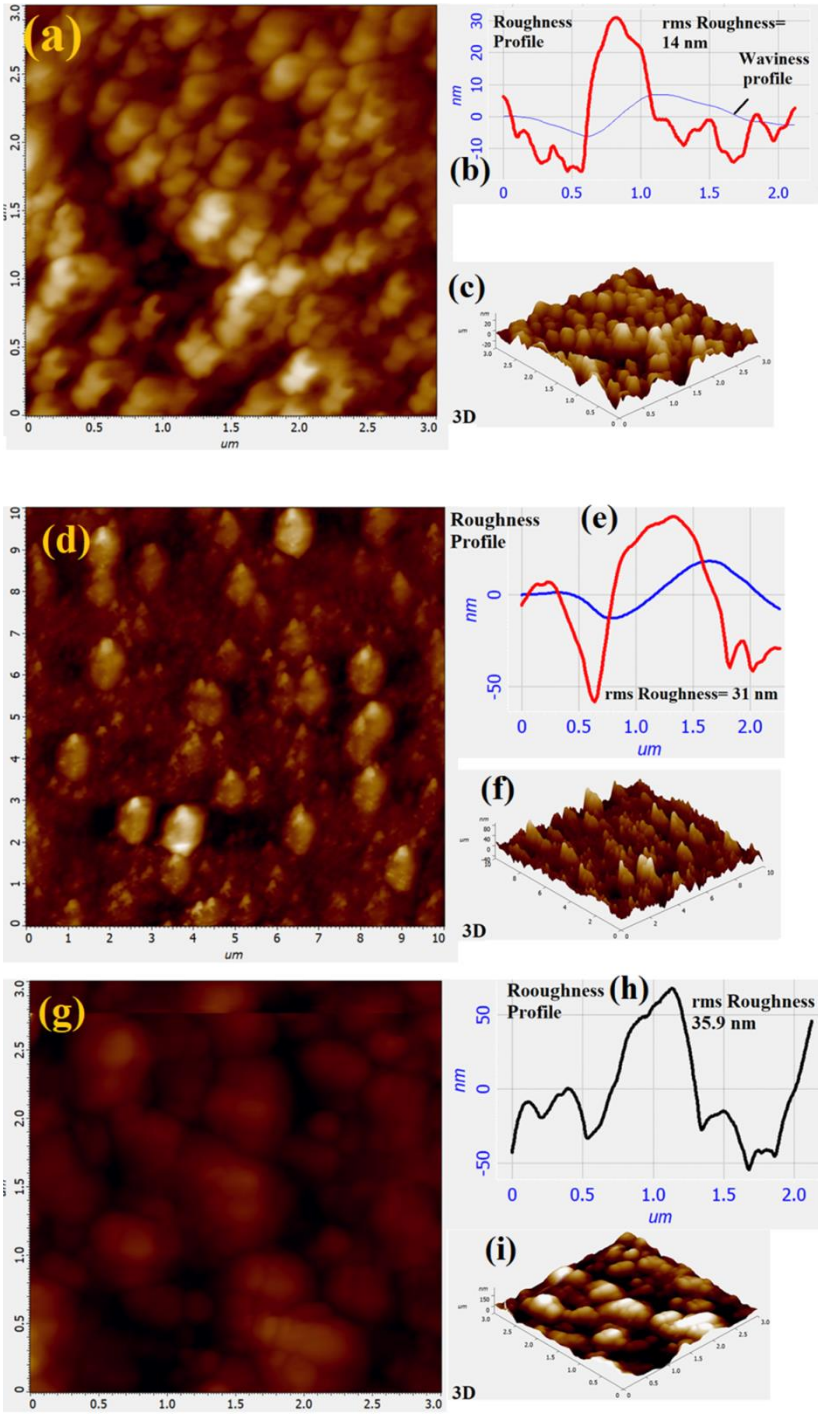

FIGURE 6.13 AFM Topography images of magnetron sputtered 0.9KNBNN thin films deposited at (a) 50W, (d) 100W and (g) (50W+100W) in two step, and their respective roughness profiles are shown in (b) (e), (h). Fig (c), (f), and (i) are showing the respective 3-D images.

The PFM topography, amplitude and PFM phase images of 0.9KNBNN thin film were recorded to study the local ferroelectric behavior of the films and the microstructure. Here, we are able to image the ferroelectric domains of 0.9KNBNN thin film using PFM, as it is highly sensitive to the loss of center of symmetry due to mechanical strain by Pt tip. Using PFM measurements, we can visualize and explain the origin of nanoscale polarization. Here, PFM is applied to 0.9KNBNN thin film to map the nanoscale polarization. Fig 6.14 shows 5 µm x 5 µm AFM image showing PFM topography, PFM amplitude and PFM phase image for 0.9KNBNN thin films, deposited on FTO coated glass substrates at 50W rf-power, when no voltage is applied and +5V & -5V is applied. The surface topography of 0.9KNBNN thin films reveal polycrystalline morphology for grains. When +5V is applied on surface of the film, the polarized surface shows bright and dark contrasts which are due to presence of polar domains distribution. The PFM phase image reveals several contrasted regions. In Fig 6.14(e) and (f), The PFM amplitude and phase contrast images indicate the presence of ferroelectric domains when +5V is applied. The bright and dark contrast shows the presence of domains with oppositely oriented polarization. Dark part shows direction of polarization opposite to applied electric field while light contrast shows polarization along the field direction. The existence of polarized ferroelectric domains in 0.9KNBNN thin film behave in similar way as p-n junction for photovoltaic application, which help to separate the photo excited electron and hole pairs. Thus, these polarized ferroelectric domains (akin to p-n junctions) decrease the charge recombination and increase the photocurrent. With changing the applied voltage from positive to negative, the contrast of regions is changed which is signature of presence of ferroelectric response in the film.

Fig. 6.15 (a) shows the PFM image of 0.9KNBNN thin film obtained at +5V. This image shows irregularly-shaped regions with bright and dark contrast. The boundaries can be seen in between the two opposite polarized region which is called domain wall and is mentioned by cross section profile in Fig 6.15 (b). Fig 6.16 shows the magnetic force microscopy (MFM) image of 0.9KNBNN films which demonstrate the magnetic response from nanoscale region of KNBNN film at room temperature. From image, we can say that a continuous magnetized area with few stray field patterns is present in the film.

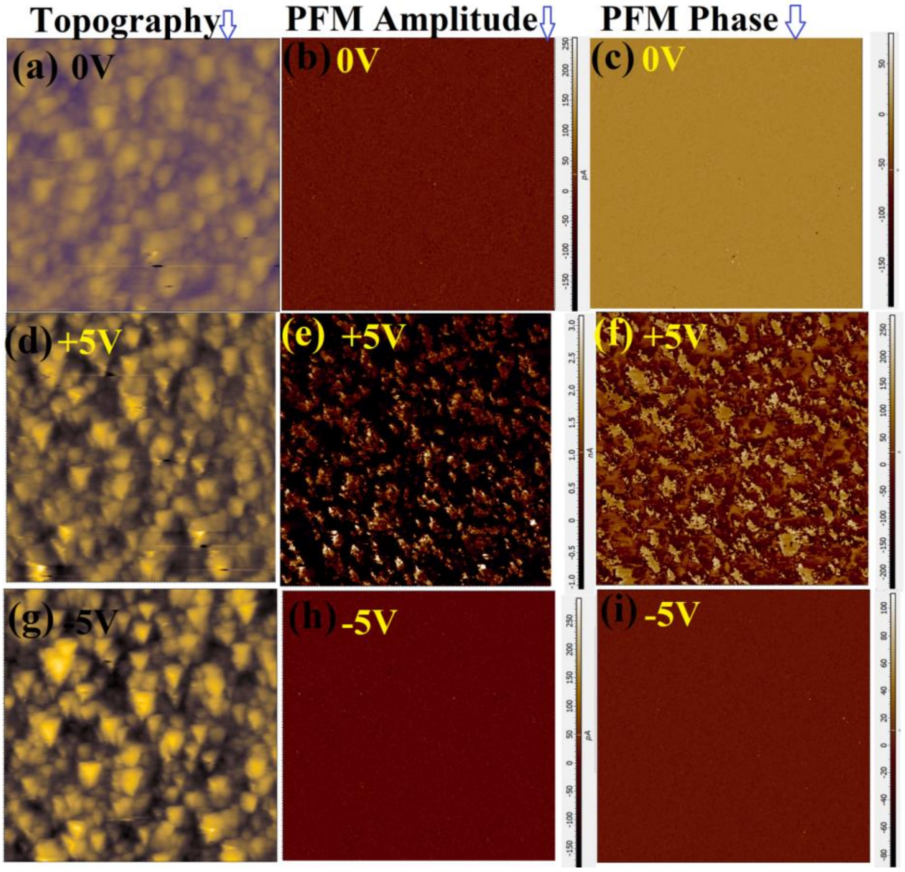

FIGURE 6.14 (a) Topography, (b) PFM amplitude and (c) PFM phase of 0.9KNBNN thin film obtained at 0V. Topography (d) Amplitude (e), phase image (f) obtained at +5V and topography (g), amplitude (h), phase image (i) obtained at -5V for 0.9KNBNN thin film deposited on FTO coated glass substrates at 50W.

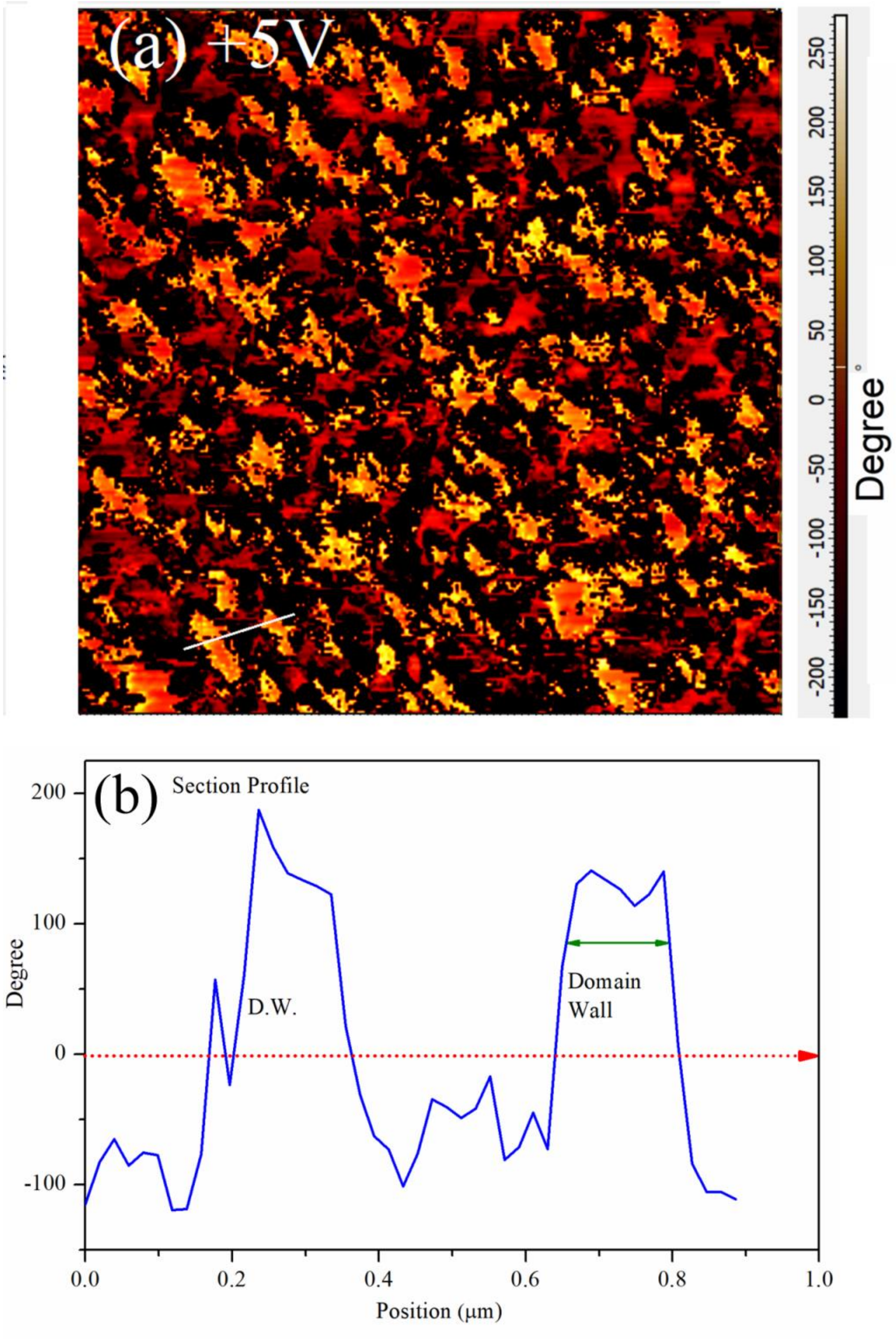

FIGURE 6.15 The PFM phase image of 0.9KNBNN film (a) obtained at +5V and section profile (b) shows the position of domain wall (D.W.). Section profile of phase image obtained at +5V, for 0.9KNBNN thin film deposited on FTO coated glass substrates at 50W rf-power.

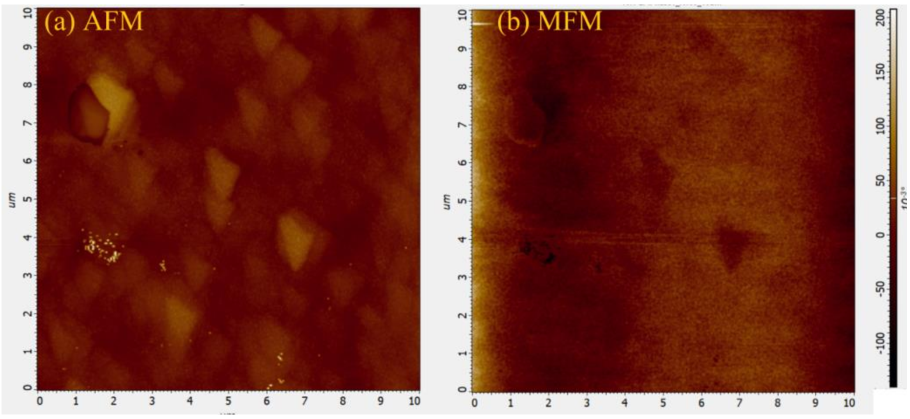

FIGURE 6.16 The MFM (a) amplitude and (b) phase image of 0.9KNBNN film

6.3.7 Current-voltage characteristics in KNBNN /FTO heterostructure

The current-voltage (I-V) characteristics of magnetron sputtered 0.9KNBNN thin films were measured using Au and Ag electrodes deposited thermally on film surface. A current-voltage curve under dark and light conditions for Au/KNBNN/Si heterostructure is shown in Fig. 6.17(a). It is observed from I-V curve that 0.9KNBNN film shows very low dark current. When device is illuminated with white light (100W power), the increased photocurrent is observed. The increase in photocurrent is due to enhancement in conductivity resulted from light induced charge carriers under light source. Fig. 6.17(b) shows the photo-response of Ag/KNBNN/FTO heterostructure upon light switching ON and switching OFF. When light is incident on KNBNN surface the electron-hole pairs are generated and can be described by the equation $h\nu \rightarrow e^- + h^+$. After separation of photo-generated charge carriers, holes get transported towards surface and recombine with O_2^- ion. In this process ($O_2^- + h^+ \rightarrow O_2$ (g)), the unpaired electrons accumulate gradually with time until the desorption and re-adsorption of oxygen attains an equilibrium state. This accumulation of electrons will increase the conductivity of surface and also increase the photocurrent till a saturation reached [J. Zhou et al. (2009)]. The photocurrent density increases from 0.042 mA/cm^2 to 0.10 mA/cm^2 within 0.15 sec upon light illumination. When light is switched OFF,

J_{sc} reduced to 0.05 mA/cm^2 within 0.11 sec. The slow decay of light during OFF condition can be attributed to presence of trap levels in the form of oxygen vacancies [Y. Jin et al. (2008)]. The origin of oxygen vacancies in KNBNN film may be attributed to Nb-ion which form an adsorption site by oxygen molecules. The Nb^{5+} ion with oxygen vacancy form the [Nb^{5+}(B′)-$V^{\cdot\cdot}_{o}$-$Nb^{5+(}$B″)] configuration. The formation of oxygen vacancies is related to doping percentage of Nb^{5+} cations on B′ sublattice in ABO_3 perovskite structure [X. Zhao et al. (2008)]. The absorbed oxygen molecules on KNBNN film surface may act as electron acceptor in dark condition and could capture the electrons during light switching OFF process and can result in slow photocurrent decay. During light illumination, the O^-_2 ions attract holes and are neutralized by them. Thus, accumulated electrons increase the conductivity. This accelerates the electron-hole pairs separation [L. Yu et al. (2017)].

The current density–voltage (J-V) characteristics of the Au/KNBNN/FTO heterostructure under light illumination are shown in Fig 6.18(a). In order to measure the effect of depolarization field, I-V is measured for unpoled, positively poled and negatively poled samples. The open circuit voltage depends on net internal field of the heterostructure. In ferroelectric based heterostructure, the net internal field is combination of both depolarization field and built-in electric field due to Schottky interface. In negative poled condition, device shows Jsc = 0.0075 mA/cm^2 and V_{oc} = -0.158mV which increased to J_{sc} = 0.02639 mA/cm^2 and V_{oc} = -0.844mV after positive poling. The observed change in I_{sc} and V_{oc} due to poling conditions confirms the effect of depolarization field on photovoltaic phenomenon.

Fig. 6.18 (c) shows the J-V curve of the Ag/KNBNN/FTO device structure. In unpoled conditions, the J_{sc} = 0.00925 mA/cm^2 and V_{oc} = 0.546 mV. In negative poled condition, device shows J_{sc} = 0.032 mA/cm^2 and V_{oc} = -0.982mV which decreased to J_{sc}

= 0.005 mA/cm^2 and V_{oc} = -0.307mV after positive poling. The observed change in I_{sc} and V_{oc} confirm the effect of depolarization field on the photovoltaic phenomenon. The observed PV effect in Ag/KNBNN/FTO device can be attributed to depolarization field in KNBNN thin film and Schottky barriers at KNBNN/Ag and KNBNN/FTO interfaces. The formation of Schottky barrier at ferroelectric/electrode interface is due to difference in their work function which create interface offset potential at interface. This is the reason why we see the opposite response of the poling field for Au/KNBNNN/FTO and Ag/KNBNNN/FTO films as shown in Fig.6.18(a) and (c).

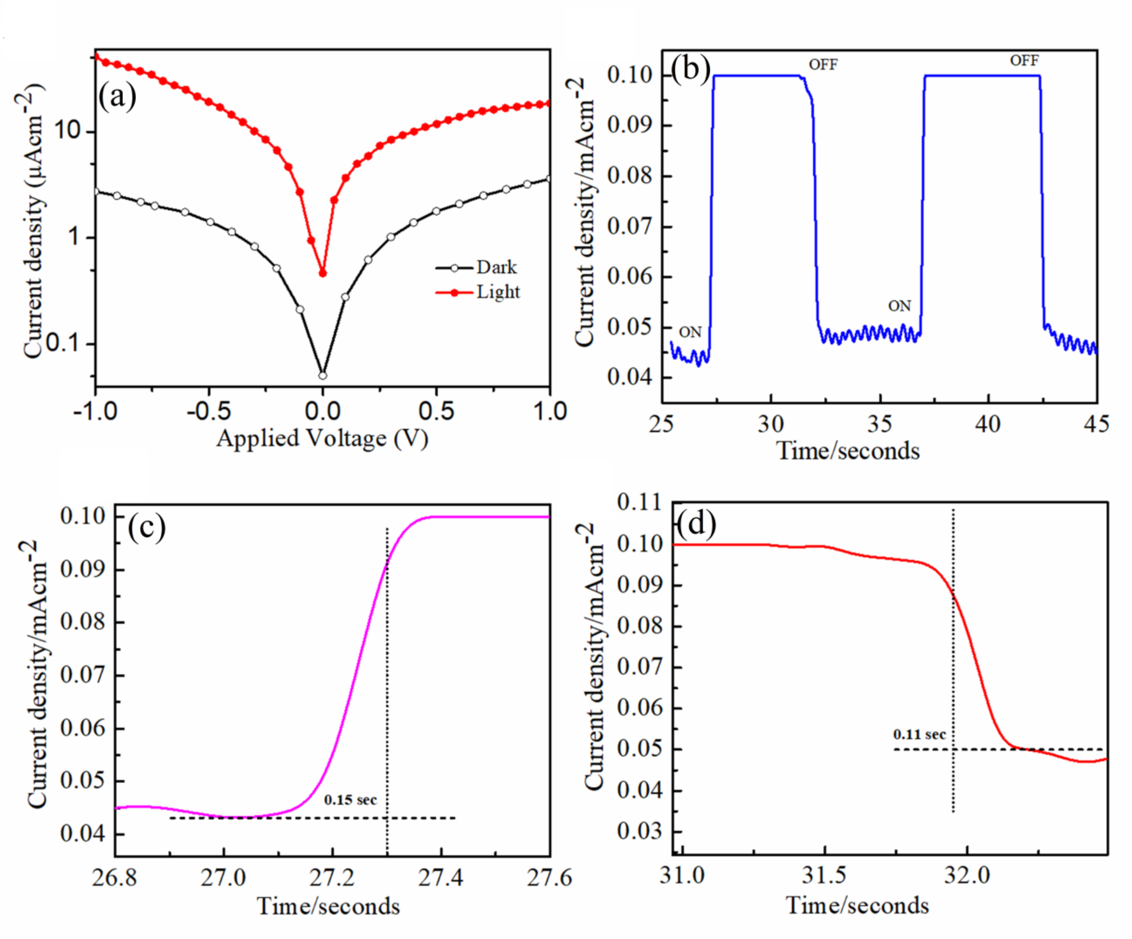

FIGURE 6.17 (a) Semi log plots of Au/KNBNN/Si device in Dark and light (b) Time dependent photocurrent response of Ag/KNBNN/FTO device under light illumination. (c) Rising edge and (d) decaying edge after enlarging the I-t curve.

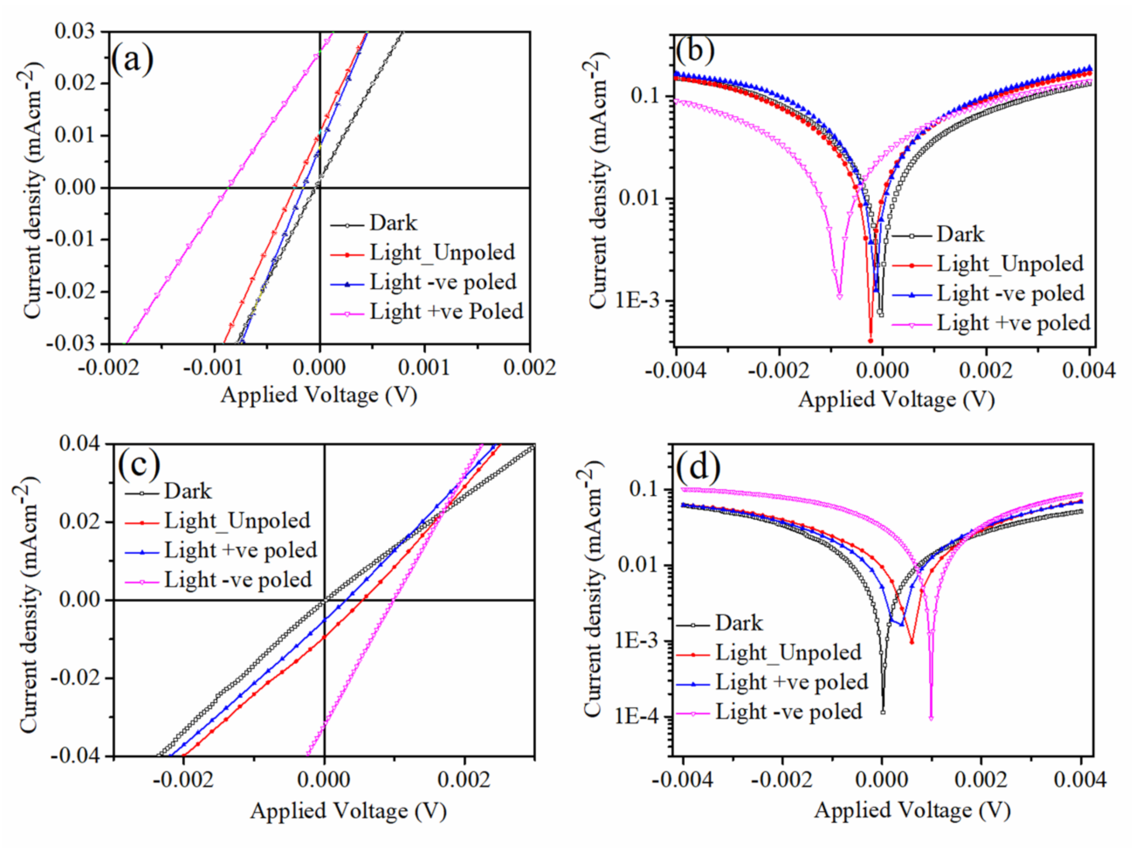

FIGURE 6.18 J-V curve of (a) Au/KNBNNN/FTO (c) Ag/KNBNN/FTO heterojunction devices in dark and under light illumination. (b) and (d) show the semi log plots of curves presented in (a) and (b).

6.3.8 Sol-gel deposited (1-x)$KNbO_3$-xBa($Ni_{1/2}Nb_{1/2}$)O_3 Thin Films as photoactive layer

After investigating the magnetron sputtered films, we tried to investigated the KNBO-BNN thin films deposited by more easy and economical method i.e. sol-gel. The KNBO-BNN thin film precursor was prepared by Pechini method as illustrated in section 2.5.3. The precursor solution was made using K_2CO_3, Niobium Oxalate, Bismuth Nitrate and Nickel Nitrate. KNBO-BNN thin films were spin-coated on ZnO nanostructure /FTO substrates. After spin coating, KNBO-BNN films were processed for rapid thermal annealing. For metal electrode, the silver thin film was thermally deposited on top of KNBO-BNN film. The thickness of Ag electrode was around 100 nm. Fig. 6.19 (a) presents the XRD pattern of as deposited 0.9KNBNN thin film which is indexed to the orthorhombic crystal structure. The surface SEM image of 0.9KNBNN thin film is shown in Fig. 6.19 (b) which confirms that film is well crystallized and has dense microstructure. The surface roughness of film is investigated using AFM as shown in Fig 6.19 (c). The sol-gel deposited 0.9KNBNN thin films have, relatively high surface roughness, as compared to the magnetron sputtered thin film. This is further illustrated by 3-D AFM image of the surface shown in Fig. 6.19 (d). The presence of domains in PFM image confirms the nanoscale ferroelectric polarization in sol-gel deposited 0.9KNBNN thin film as shown in Fig. 6.19 (e). The optical band gap of 0.9KNBNN thin film is (~ 1.28 eV) which is much lower than the $KNbO_3$ thin film (~3.45eV) as shown in Fig. 6.19 (f).

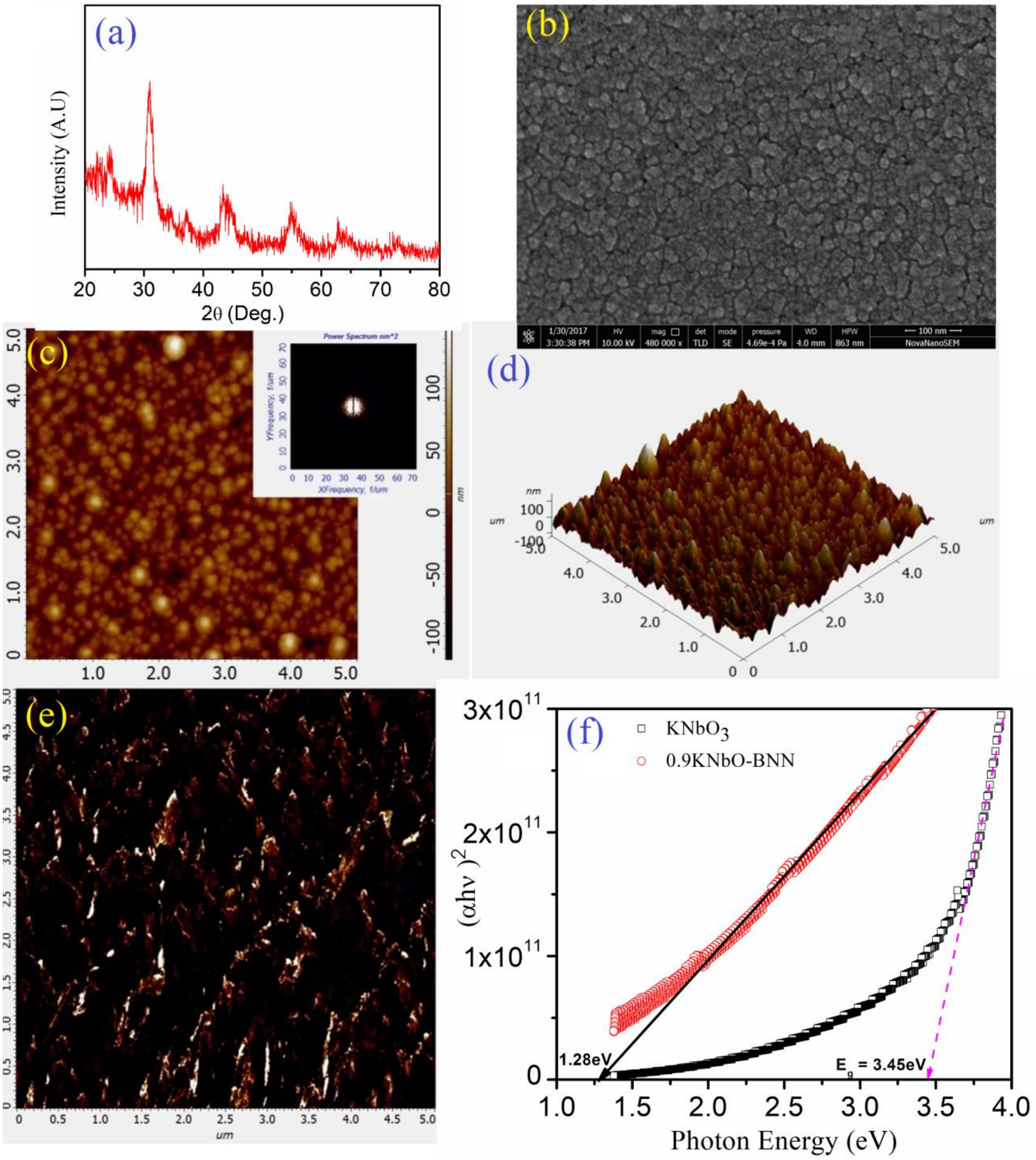

FIGURE 6.19 (a) XRD pattern (b) SEM image (c) AFM topography, Inset is showing the FFT spectra of image (d) 3-D image of AFM (e) PFM image showing ferroelectric domains and (f) Tauc plots for band gap of sol-gel deposited 0.9KNBNN thin films.

6.3.9 ZnO Nano-Structures as light trapping layer for KNBNN Solar Cells Application

Zinc Oxide is the most widely developed and investigated nanomaterial for variety of advanced technological and device applications. The unique characteristics of the ZnO is that it can be grown very easily into different morphology nanostructures just by changing the process variables which in turn modifies its physical behaviour. In view of this, we decided to explore the ZnO nanostructure as a light trapping layer on the photo-ferroelectric thin film device to further enhance the photovoltaic response. The three types of ZnO nanostructures viz. nanoparticles, nanowalls and nanorods were investigated in this work. The details of ZnO nanostructure synthesis, device fabrication and their characterization are given in the following sections.

6.3.9.1 Synthesis of ZnO nano-Structures

The ZnO nanoparticles were synthesized by the ultrasonic method [W. Yang et al (2016)]. Stoichiometric amount of zinc acetate dihydrate was dissolved in 100 mL of ethyl alcohol and kept for ultrasonic dispersion for 30 minutes, and appropriate amounts of polyethylene glycol (PEG-400) was added in this solution-1, with further 1h of ultrasonication. In another beaker, Solution-2 was prepared by mixing 0.84 g LiOH in 50 mL ethyl alcohol with ultrasonication for 30 min. After that, both solution-1 and solution-2 were mixed. The ZnO nanoparticles were obtained after continuous ultrasonication at 40^{o}C for 30 min. In obtained solution, 0.6 mL of oleic acid was added, and the mixture was centrifuged for 15 min at 3000 rpm. The obtained sediment was washed with ethanol to get the ZnO. After removing unreacted solvent materials from white residue, the ZnO nanoparticles were dispersed in n-hexane. These nanoparticles were coated on substrates using a spin coater to prepare the thin film for device applications. The schematic diagram of nanoparticles synthesis process is shown in Fig.6.20.

ZnO nanorods and nanowalls were synthesized by seed-mediated method [C.-H. Hung et al. (2003); Z. Liang et al. (2013)]. The Zinc Oxide nanorods and nanowalls were grown on glass substrates and FTO coated glass substrates by using a chemical solution deposition process. Prior to deposition of seed layers, substrates were ultrasonicated using de-ionized water, acetone and ethanol, respectively, and kept for drying at 200 ^{o}C in oven. For ZnO seed layer deposition, pure ZnO disc was used as a target. Argon was used as a process gas. ZnO films were deposited at 70% duty cycle and 15 sccm Ar flow rate by using sputter coater. Zinc Nitrate Hexahydrate and hexamethylenetetramine were mixed with DI water to make precursor solution for nanorods and nanowalls growth. The seed layers coated substrates were immersed in precursor solution. For ZnO nanorods growth, the solution was maintained at 90^{o}C with pH around 6. ZnO nanowalls were grown at 50^{o}C temperature. The chemically processed glass and FTO substrates were annealed in air at 200 ^{o}C for 2 hours. Fig. 6.21 shows the schematic Diagram of ZnO nanostructures process set-up. For photovoltaic device fabrication, ZnO nanorods and nanowalls were grown on FTO substrates.

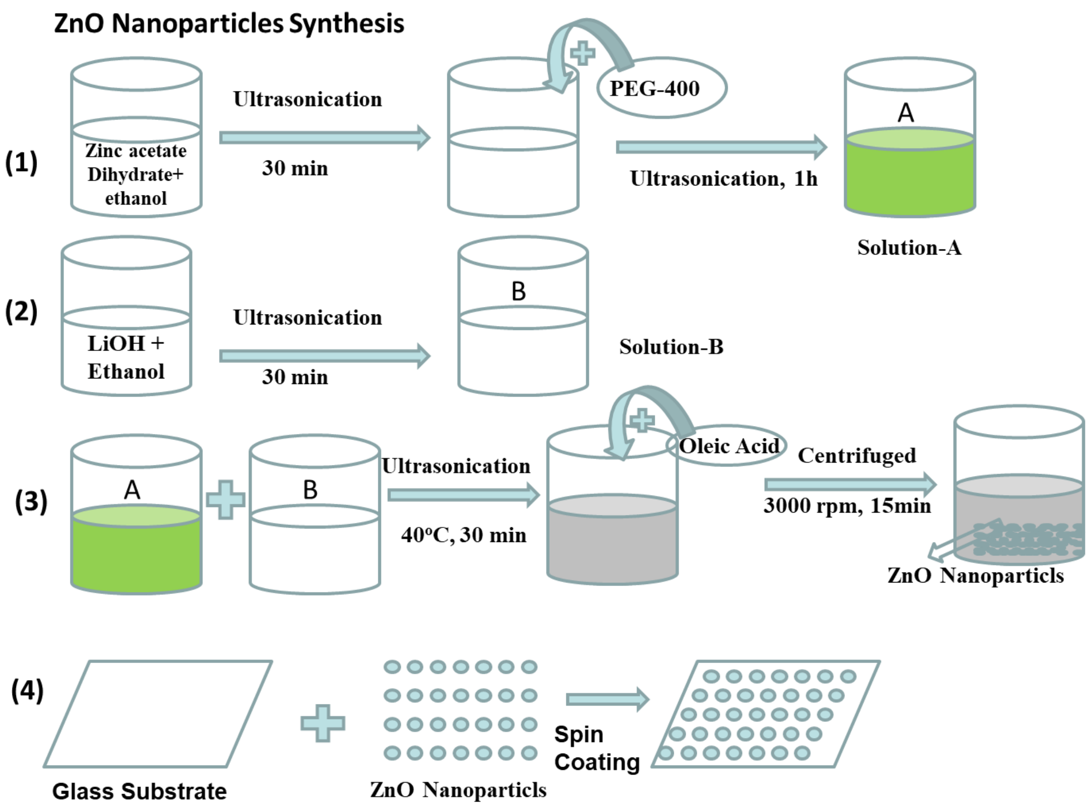

FIGURE 6.20 Schematic diagram for ZnO nanoparticles synthesis and their coating on substrates.

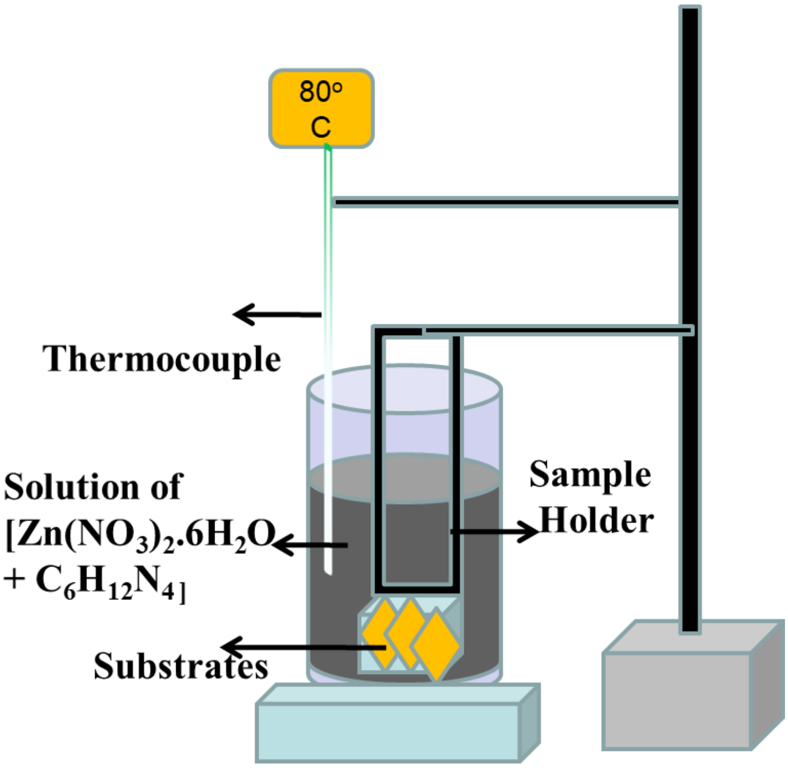

FIGURE 6.21 Schematic diagram of ZnO nanostructures process set-up.

6.3.9.2 Structural and Morphological properties of ZnO nano-Structures

The surface morphology of the as-grown ZnO nanoparticles, nanowalls and nanorods on glass and FTO coated glass substrates are analyzed using SEM, HRTEM and AFM. As shown in Fig. 6.22(a), the TEM image suggests that the ZnO nano-particle sizes vary from 1.8 nm to 2.9 nm. Fig.6.22 (b) shows the HRTEM images of as synthesized ZnO nanoparticles. The SAED pattern of ZnO nanoparticles is presented in Fig. 6.22 (c). It is observed that as grown nanoparticles are highly crystalline. Fig. 6.23 (a) illustrates the top view HRSEM image of ZnO nanorods grown on FTO glass substrates.

Fig. 6.23 (a) shows the HRSEM Image of the as grown ZnO Nanorods on FTO glass substrate. The grown nanorods are well aligned and vertical except few of them are tilted but can be used well for device application. The diameter of ZnO nanorods is about 65-100 nm, and the average length is 300-600 nm. Fig. 6.23 (b) shows the HRTEM image of single ZnO nanorod. Single nanorod characterized by HRTEM has diameter ~70 nm and length ~328 nm. Fig. 6.23 (c) & (d) depict HRTEM image of ZnO nanorod showing hexagonal shaped cross-section. The crystalline nature of ZnO nanorods is further confirmed by SAED pattern shown in Fig. 6.23 (f). Fig. 6.23(e) illustrates the surface morphology of as grown nanorods. The HR-TEM images and SAED patterns of ZnO nanorods confirm the crystalline and defect-free nature. The lattice fringes have interplanar spacing around 0.29 nm. The interplanar spacing values obtained are well related with d spacing of (002) lattice plane as obtained from XRD. The SAED patterns of ZnO nanorods with circular ring patterns confirmed its polycrystalline nature as supported by the XRD data.

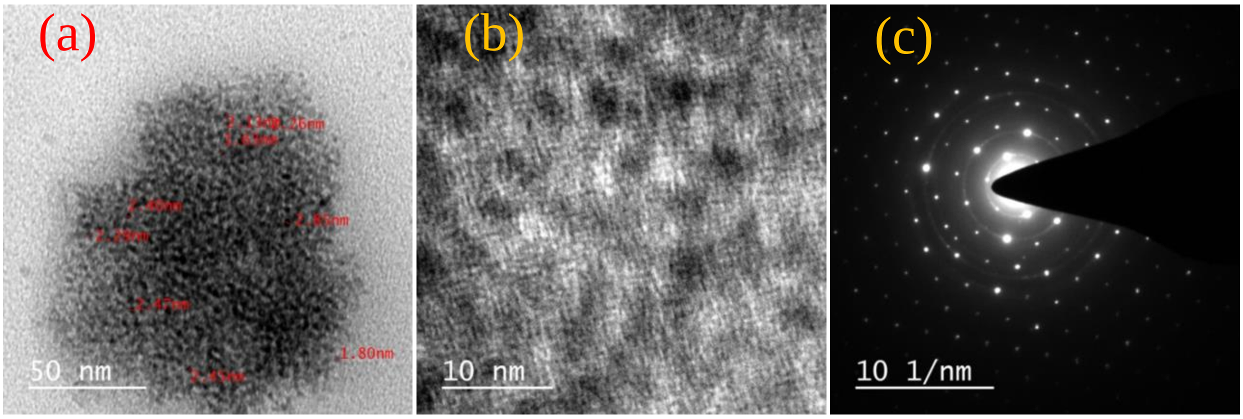

FIGURE 6.22 (a) TEM image of ZnO Nano-particles (b) HRTEM image (c) SAED pattern of ZnO nanoparticles.

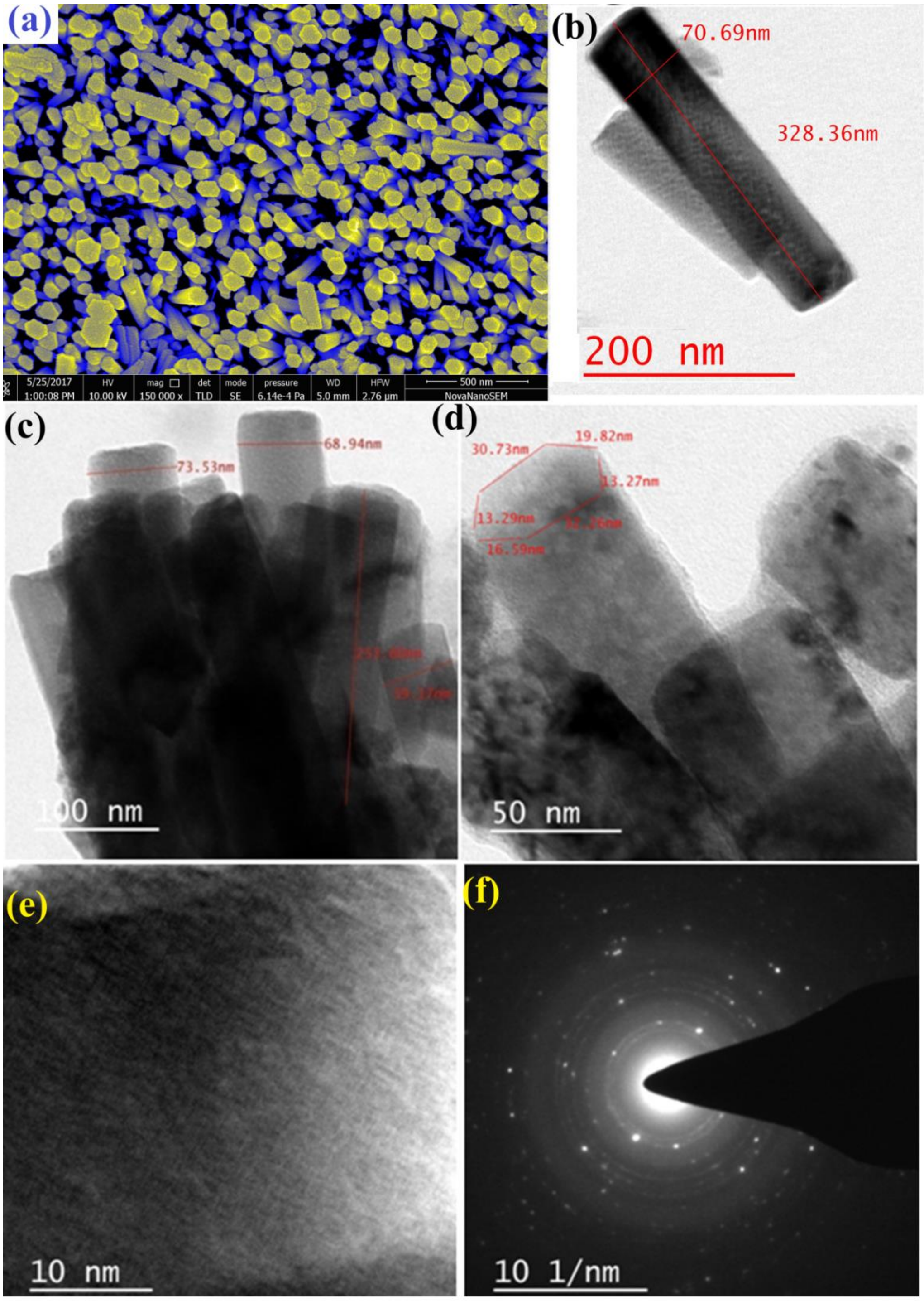

FIGURE 6.23 (a) HRSEM Image of as grown ZnO Nanorods on FTO glass substrate, (b) HRTEM image of single Nanorod, (c) & (d) HRTEM image of ZnO Nanorod showing its hexagonal cross-sectional shape, (e) Surface morphology of Nanorod (f) SAED pattern of ZnO nanorods confirming crystalline nature,.

Figs.6.24 (a), (b) and (c) show the AFM morphology, roughness profile and 3-D image, respectively, of as grown ZnO nanorods array on FTO glass substrate. The well aligned growth of nanorods and nanowalls is due to initial ZnO seed layer which is uniformly deposited on substrate by magnetron sputtering. The excellent crystalline nature of ZnO seed layer provides well aligned grains for nanorods growth. The ZnO surface is polar in nature and is either positively or negatively charged. The charged surface of ZnO seeds will attract the OH$^-$ or Zn$^+$ ions on its surface. These ions will cover the ZnO seed surface and further attract the other ions with opposite sign which can react with them to form ZnO and contribute to the growth of ZnO nanorods. The growth direction of nanorods depends on the direction of dipole moment [Q. Li et al. (2005)].

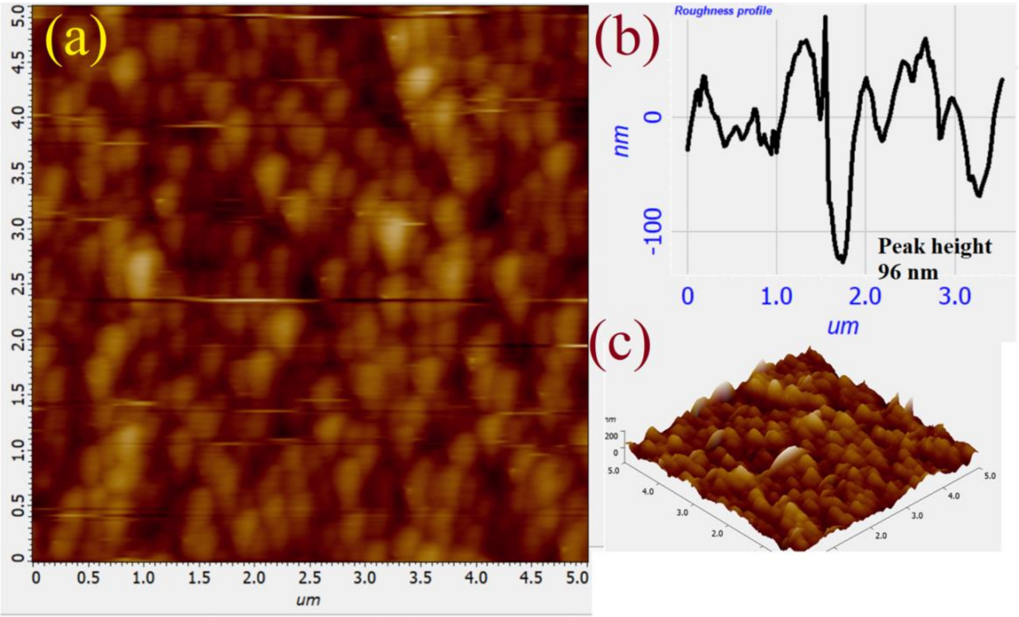

FIGURE 6.24 (a) AFM surface morphology (b) roughness profile and (c) 3-D image of ZnO nanorods grown on FTO substrate.

Detailed characterization of as grown ZnO nanowalls on glass substrate is presented in Fig.6.25. Fig.6.25 (a) shows the HRSEM image (b) Enlarged view of nanowalls (c) Shape of nanowall showing side width (d) HRSEM image showing the single ZnO nanowall (e) HRTEM image of ZnO nanowalls and (f) SAED pattern of ZnO nanowalls. The width of ZnO nanowalls are in the range of 2.4 μm to 2.6 μm and depth is in the range of 300 nm to 570 nm. The thickness of nanowalls is found in the range of 7 nm to 14 nm as shown in Fig. 6.25 (e). From the TEM image shown in Figs. 6.25 (d) & (e), we can observe that external surface of the nanowalls is continuously grown structure. The inner area surrounded by nanowalls is hexagonal and triangular in shape. Single crystal selected area electron diffraction (SAED) patterns from individual nanowall confirms the crystalline nature.

Figs. 6.26 (a), (b) and (c) show the X-ray diffraction patterns of the ZnO nanoparticles, ZnO nanorods and ZnO nanowalls, respectively, with their corresponding SEM images. All the diffraction patterns can be indexed to the standard hexagonal wurtzite type phase of ZnO. The diffraction peaks at the scattering angle (2θ) of 31.37, 35.89, 56.34 corresponds to the reflection from (100), (101), (110) crystal planes of hexagonal structure of ZnO, respectively (JCPDS-ICDD card No. 05-0664). It can be seen from Fig. 6.26 (b), (c), that the (002) diffraction peak of the XRD pattern has the stronger intensity as compared to other peaks. It confirms that nanorods and nanowalls have a preferred orientation along the c-axis. The intensity of (002) diffraction peak is even more strong for ZnO nanorods than ZnO nanowalls.

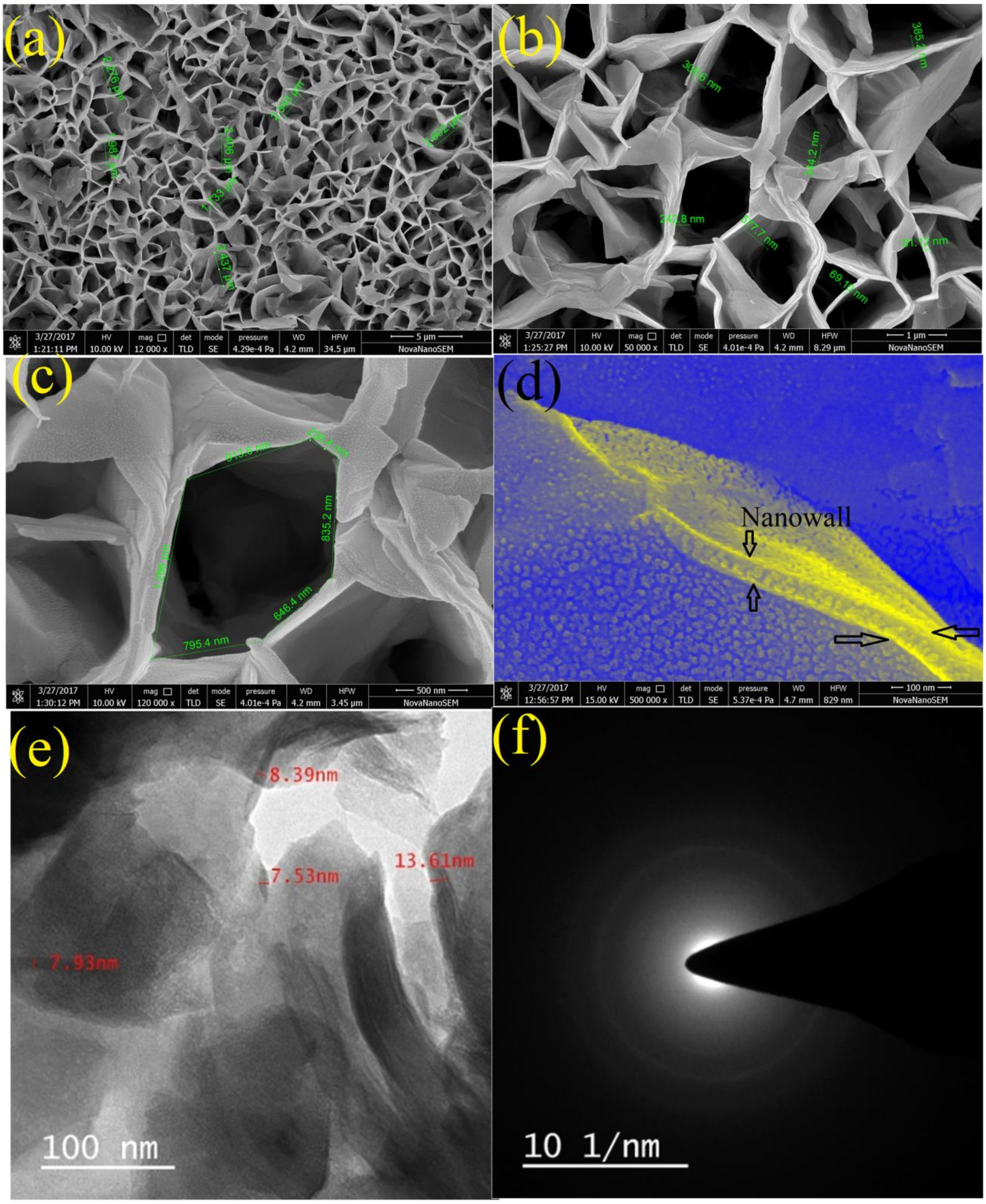

FIGURE 6.25 (a) HRSEM Image of as grown ZnO nanowalls on glass substrate (b) Enlarged view of nanowalls (c) Shape of nanowall showing the side width (d) HRSEM image showing the single ZnO nanowall (e) HRTEM image of ZnO nanowalls and (f) SAED pattern of ZnO nanowalls.

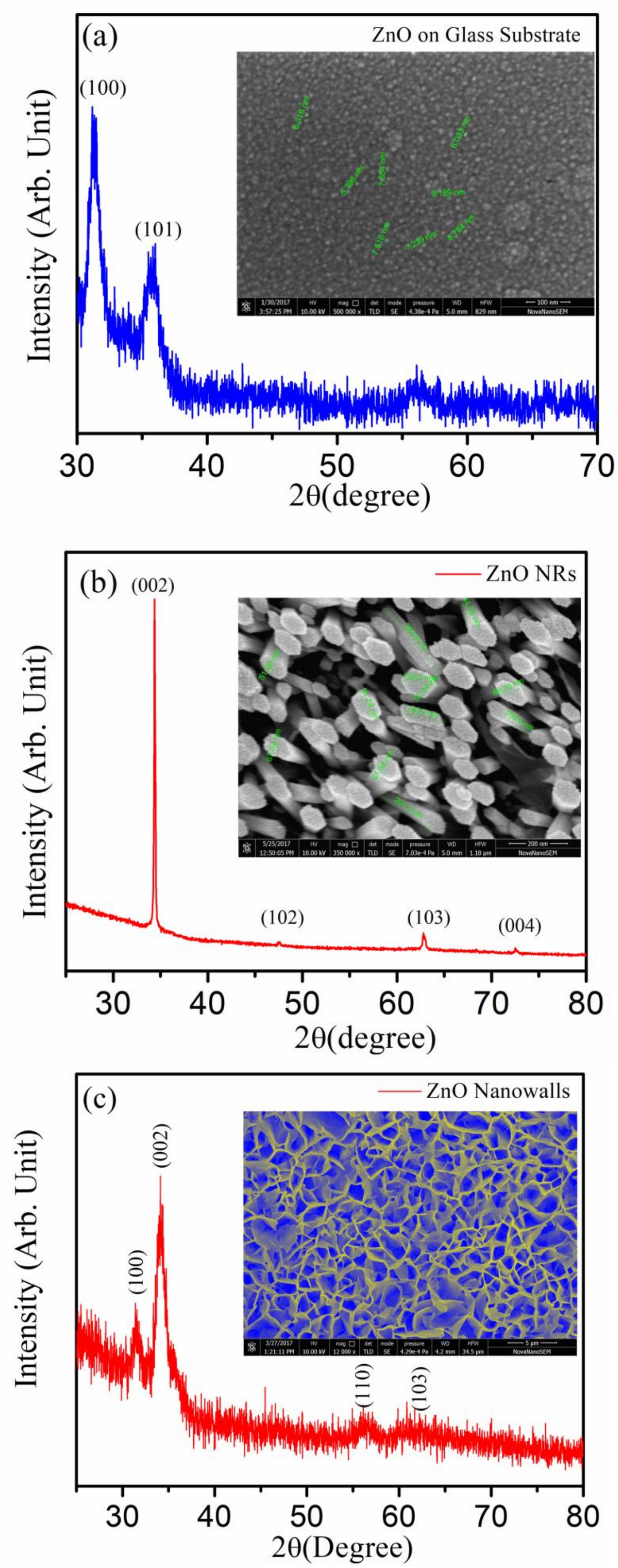

FIGURE 6.26 XRD patterns of (a) ZnO particles (b) ZnO nanorods and (c) ZnO nanowalls. Inset of figures shows the corresponding SEM image.

6.3.9.3 Growth Mechanism of Nanowalls and Nanoscale Characterization using AFM

Considering as an essential light trapping layer for solar cells, the growth mechanism of nanostructured materials needs to be well understood by microstructural analysis. ZnO nanostructures were subjected to AFM study to determine the surface roughness and topographies. Fig. 6.24 and Fig. 6.30 Show the surface topography of the ZnO nanorods, nanoparticles, and nanowalls. Fig.6.30 (a) shows the AFM surface topography of ZnO nanoparticles. The rms roughness of ZnO nanoparticles is around 5 nm. ZnO nanorods and nanowalls indicate much coarser surface roughness compared to nanoparticles. At nucleation stage, the ions try to attain a stable position on the substrate using their self-energy and thermal energy of the substrate. The atoms and ions start interacting with surrounding atoms and ions through surface diffusion and migration. With time, these atoms and ions starts bonding with each other and follow a particular pattern depending on their growth orientation. The schematic diagram of growth study of ZnO nanorods and nanowalls are shown in Fig.6.27 and in Fig.6.28 respectively. This growth phenomenon of ZnO nanowalls are further confirmed by AFM microscopy. From AFM analysis, it is observed that surface roughness of ZnO nanorods is around 22 nm while nanowalls have roughness around 135 nm. There are four stage are studied by AFM to analyse the growth mechanism of ZnO nanowalls and AFM images are shown in Fig.6.30. From AFM analysis, it is found that roughness increases from 5 nm to 135 nm. Another statistical parameter is used to study the distribution of peaks and valley is skewness. The skewness parameter shows a positive value which suggest that walls grow in vertical direction. The decrease in profile peak density shows that with increasing time ZnO nanowalls interconnected and have large size which is confirmed by its AFM image shown in Fig. 6.30 (d).

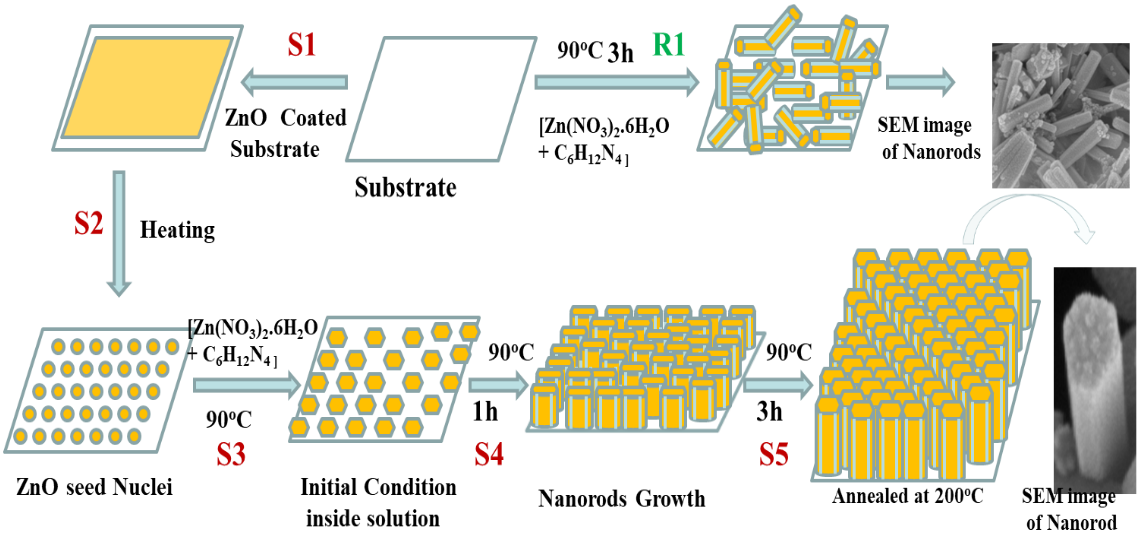

FIGURE 6.27 Schematic diagram showing synthesis steps of ZnO Nanorods growth process.

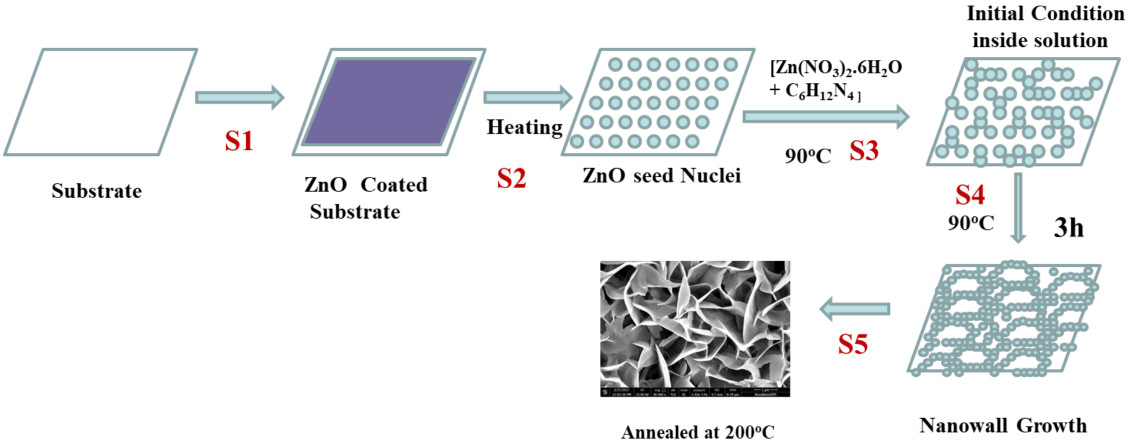

FIGURE 6.28 Schematic diagram showing synthesis steps of ZnO Nanowalls growth process.

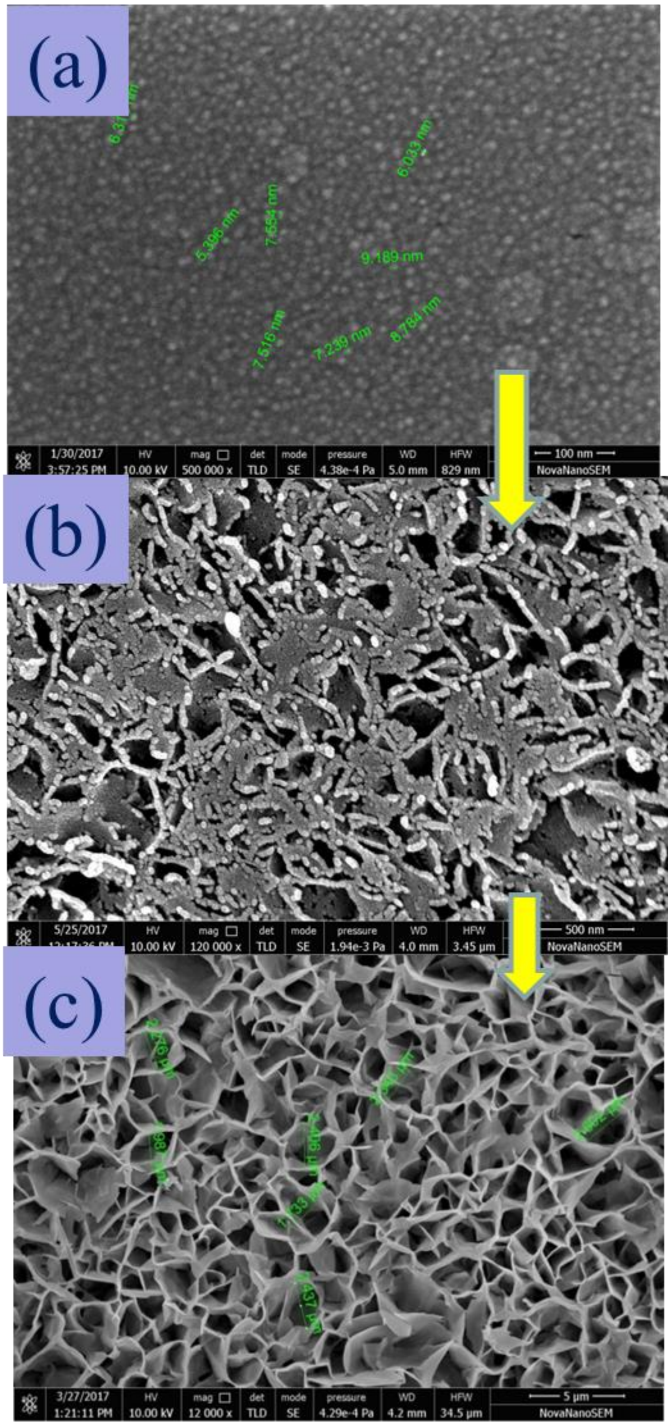

FIGURE 6.29 SEM image of (a) initial stage (b) intermediate stage and (d) final stage of as grown ZnO nanowalls on glass substrate

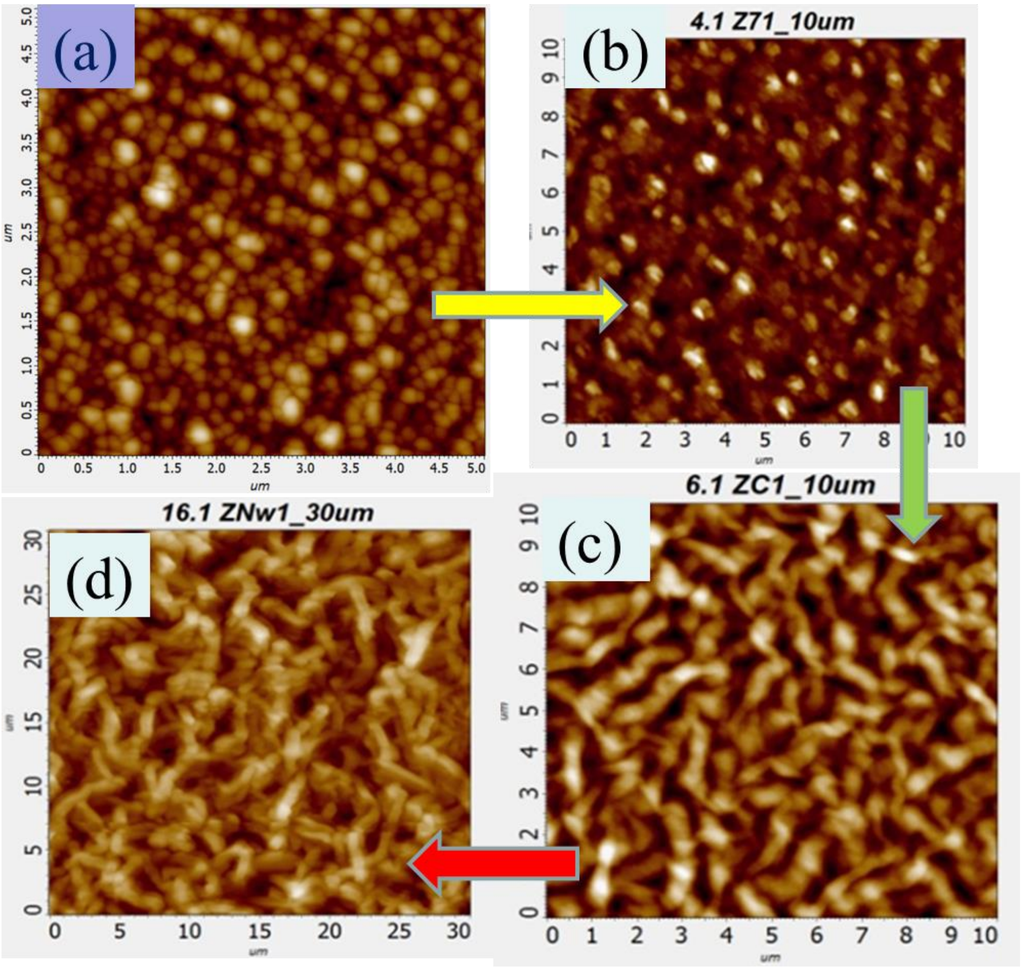

FIGURE 6.30 AFM images of (a) initial stage (b) after 30 minutes (c) intermediate stage and (d) final stage of as grown ZnO nanowalls on glass substrate

6.3.9.4 Light Trapping behavior of ZnO nano-Structures

The UV-visible absorption spectroscopy was employed to analyze the optical properties of ZnO nanostructures grown on FTO glass substrates. Fig. 6.31(a) shows the %Transmittance and % Reflectance of ZnO nanoparticles, nanorods and nanowalls under identical conditions. The spectra are plotted in the wavelength range from 200 nm to 1000 nm. The %Transmittance of ZnO nanostructures is more than 80% and % Reflectance is below 20%. Fig. 6.31(b) shows the percentage reflectance of bare FTO glass substrate, KNBNN thin film with and without ZnO nanowalls grown on FTO substrates. The % reflectance of FTO glass substrate reduces from 13.68% to 7.10%

after ZnO nanostructures growth. Reflectance measurement indicates that ZnO nanowalls are the excellent choice for light trapping schemes. It is observed that when KNBNN thin film are deposited on ZnO nanowalls the reflectance is reduced as compared to KNBNN film directly deposited on FTO substrate as shown in Fig. 6.31 (b).

Fig. 6.32 presents the schematic illustration of light scattering from (a) ZnO Nanoparticles, (b) Nanorods and (c) nanowalls. According to model presented in this figure, the light rays are less deviated from nanoparticles surfaces due to their circular shape and small size. There is also high probability of reflection of light from surfaces. As shown in Fig. 6.32(b), for ZnO nanorods array, the light rays are not only incident on hexagonal top surface but also on the nanorod sides, from where, there is high possibility that rays will get scattered on the surface and will be trapped by nanorods array after multiple reflections. In case of ZnO nanwalls, the light rays are incident not only on the top surface of walls but also inner surface of walls as illustrated in Fig. 6.32 (c). The advantage of nanowalls for light scattering and trapping is in its shape and morphology. The walls are very thin, so, light rays mostly strike inside surface and collide multiple times and get trapped. This is the reason why nanowalls are more useful for light trapping in solar cell devices.

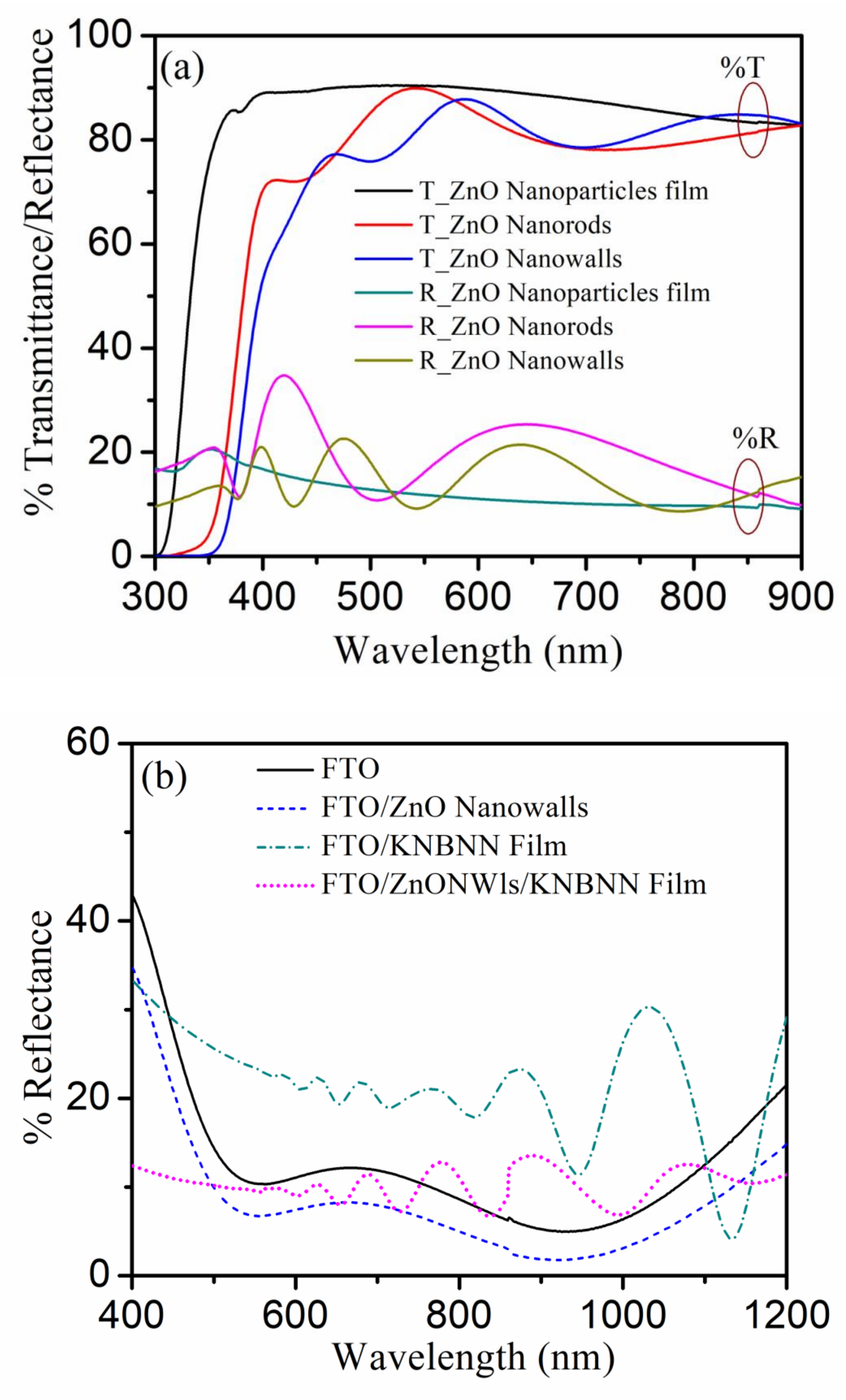

FIGURE 6.31 (a) Transmittance and reflectance of as grown ZnO nanostructures (b) Percentage reflectance of KNBNN thin film with and without ZnO nanowalls.

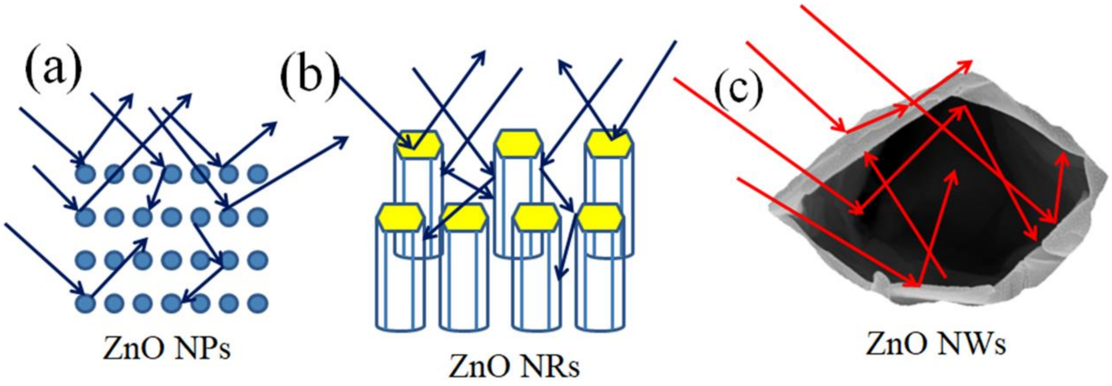

FIGURE 6.32. Schematic illustration of light scattering from (a) ZnO Nanoparticles, (b) Nanorods and (c) Nanowalls

6.3.9.5 Photo-voltaic behavior of KNBNN and KNBNN/ZnO nanostructures Heterojunction devices

In order to study the photovoltaic behavior of KNBNN thin films, the films were coated on FTO glass substrates and Ag electrode was thermally deposited on top of it. Fig. 6.33 (a) shows the schematic representation of solar cell device structure with Ag/KNBNN/FTO heterostructure. Fig. 6.33 (b) shows the schematic energy level diagram and charge transfer at the interface of Ag/KNBNN/FTO heterostructure. Owing to $\Phi_{FTO} > \Phi_{KNBNN}$, electrons will move from the conduction band of KNBNN into FTO until the Fermi levels are equalized. When light is illuminated on the device, the excitons are formed and get separated by built-in-potential. The separated charge carriers are migrated from KNBNN to Ag and KNBNN to FTO interfaces. Two different types of interfaces are formed and termed as top and bottom interface. The interface electric field helps separate the charge carriers. The electrons are excited from valence band to conduction band of KNBNN.

The current-voltage measurement was performed on Ag/KNBNN/FTO device. Fig. 6.34 shows J-V characteristics of sol-gel deposited KNBNN thin film with Ag/KNBNN/FTO heterojunction in dark and light illumination. The Inset shows (a) enlarged view of J-V curve and (b) Dark J-V for unpoled and negatively poled devices. In unpoled conditions the J_{sc} = 0.0063 mA/cm^2 and V_{oc} = 0.244 mV. In negative poled condition, device shows J_{sc} = 0.01286 mA/cm^2 and V_{oc} = 0.387 mV.

The effect of light scattering from ZnO nanostructures on KNBNN based photovoltaic devices performance was studied to know the improvement in photocurrent. In these heterojunctions, ZnO NS act as electron transport layer (ETL) and MoO_3 film act as hole transport layer (HTL). ZnO is already proven efficient ETL for organic/perovskite solar cells and due to its spontaneous polarization (4.1-7.0μC/cm^2); it might improve the power conversion efficiency of p-i-n or n-i-p devices [T. Cao et al (2018)]. Upon light illumination on this p-i-n or n-i-p junction, an improved J_{sc} and V_{oc} are achieved due to increased internal electric field.

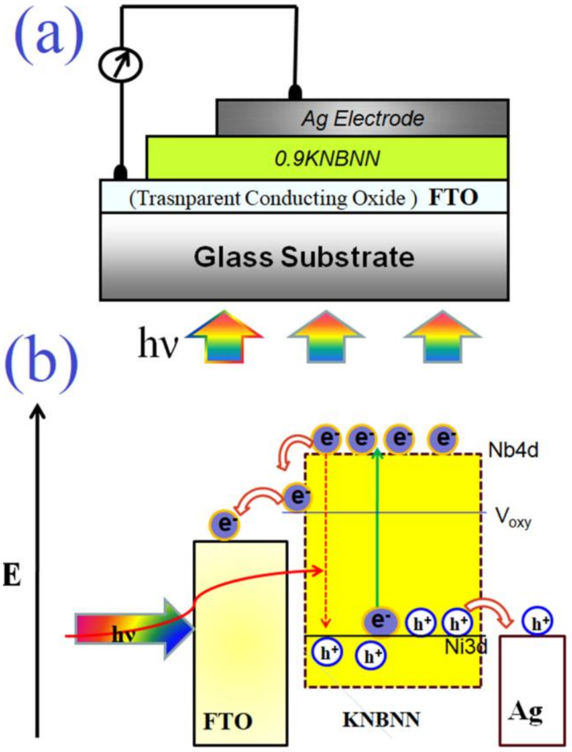

FIGURE 6.33 (a) A schematic representation of solar cell device structure with Ag/KNBNN/FTO heterostructure (b) corresponding schematic energy level diagram for single junction showing the internal photo-electric process.

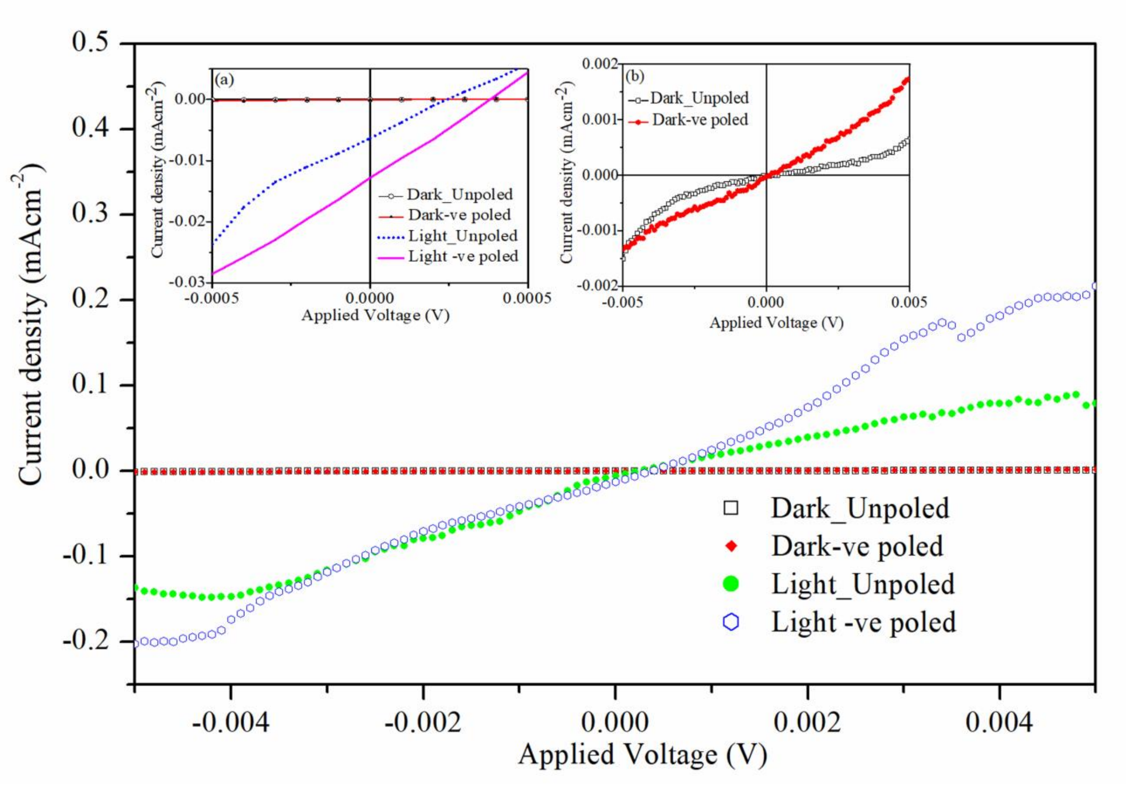

FIGURE 6.34 J-V characteristics of single KNBNN thin film with Ag/KNBNN/FTO heterojunction in dark and light illumination. The Inset shows (a) enlarged view of J-V curve and (b) Dark J-V for unpoled and negatively poled devices

The 0.9KNBNN thin films were deposited on “ZnO nanostructure coated FTO substrates” and annealed subsequently. Afterwards, MoO_3 thin film which acts as HTL, was thermally deposited on 0.9KNBNN layer. The Ag was thermally deposited subsequently which acts as electrode. Thus 0.9KNBNN film is sandwiched between ETL (ZnO) and HTL (MoO_3) layer to design a new n-i-p heterostructure. The n-i-p type solar cell with device configuration of Ag/MoO_3/KNBNN/ZnONS/FTO is presented in Fig.6.35. Three different types of devices are prepared using ZnO nanoparticles, nanorods and nanowalls to compare the effect of light trapping by these layers. Fig. 6.36 presents the J-V characteristics of KNBNN based

Ag/MoO_3/KNBNN/ZnONS/FTO heterojunction in dark and light illumination. The Inset shows the dark J-V curve for devices with varying the ZnO nanaoparticles, nanorods and nanowalls. In Ag/MoO_3/KNBNN/ZnO nanoparticles/FTO heterojunction device after negatively poling conditions, the measured J_{sc} = 0.019 mA/cm^2 and V_{oc} = 0.073 V. However, single layer KNBNN junction solar cell in negative poled condition, shows J_{sc} = 0.01286 mA/cm^2 and V_{oc} = 0.387 mV. In Ag/MoO_3/KNBNN/ZnO nanorods/FTO heterojunction device, J_{sc} = 0.038 mA/cm^2 and V_{oc} = 0.11 V. Another device with ZnO nanorods shows J_{sc} = 0.034 mA/cm^2, but V_{oc} is almost same. The photocurrent for devices with ZnO nanowalls shows increased J_{sc} = 0.067 mA/cm^2, as compared to devices with ZnO nanorods and nanoparticls. But open circuit voltage (V_{oc}) is slightly decreased for ZnO nanowalls based devices. The fill factor for all these devices is nearly 26%. So, by comparing the photocurrent, it is can be concluded that the devices containing ZnO nanowalls shows higher photocurrent as compared to ZnO nanoparticles and ZnO nanorods. The photocurrent density follows the sequence $J_{NW\text{-}KNBNN} > J_{NR\text{-}KNBNN} > J_{NP\text{-}KNBNN}$, which is consistent with their percentage reflectance obtained earlier and shown in Fig. 6.31. These results indicate that light trapping scheme can be very important factor in improving the photocurrent of photovoltaic devices.

This increased performance of device suggests that ZnO NWs provide a relatively superior contact with the photoactive layers in comparison to ZnO NPs and ZnO NRs. The rough interfaces of ZnO nanostructures improve the efficiency of devices by increasing the light harvesting in the photo-active layer and provide the conducting path for charge extraction. The higher current was observed for devices having ZnO nanostructures as electron extraction layers. The devices having ZnO NWs show more J_{sc} as compared to the devices having ZnO NRs and NPs. The reason behind higher current collection in ZnO NWs/KNBN heterostructure devices is their rougher surface, low density, high surface area and interlinking of nanowalls with each other. Rough surface reduces the reflectance of incident light and thus increases the absorption of light in the photoactive layer. From SEM and AFM images, it can be concluded that NRds also provide high roughness but their alignment is not entirely symmetrical, and few of them are tilted. The tilted nanorods block some part of incident light to reach inside photoactive layer. The drawback of the high-density nanostructure is that incident light does not properly reach to photoactive layer, so low-density nanostructured films are better to improve light absorption. ZnO nanorods are highly dense as compared to nanowalls. The higher surface area of ZnO nanowalls provides more interaction points for charge extraction. Another feature which proves ZnO nanowalls superior in electron extraction than nanorods is their interlinked structure. Interlinked ZnO nanowalls provide conducting path to increase charge carriers' mobility and prevent the defect induced charge recombination process. In contrast, ZnO nanoparticles have low surface roughness and surface area and are not much effective to improve current collection in devices.

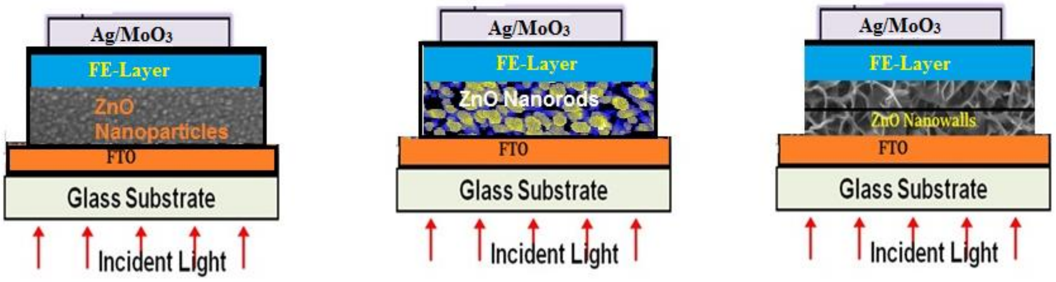

FIGURE 6.35. Schematic representation of solar cell device structure using ZnO Nanoparticles, Nanorods and nanowals

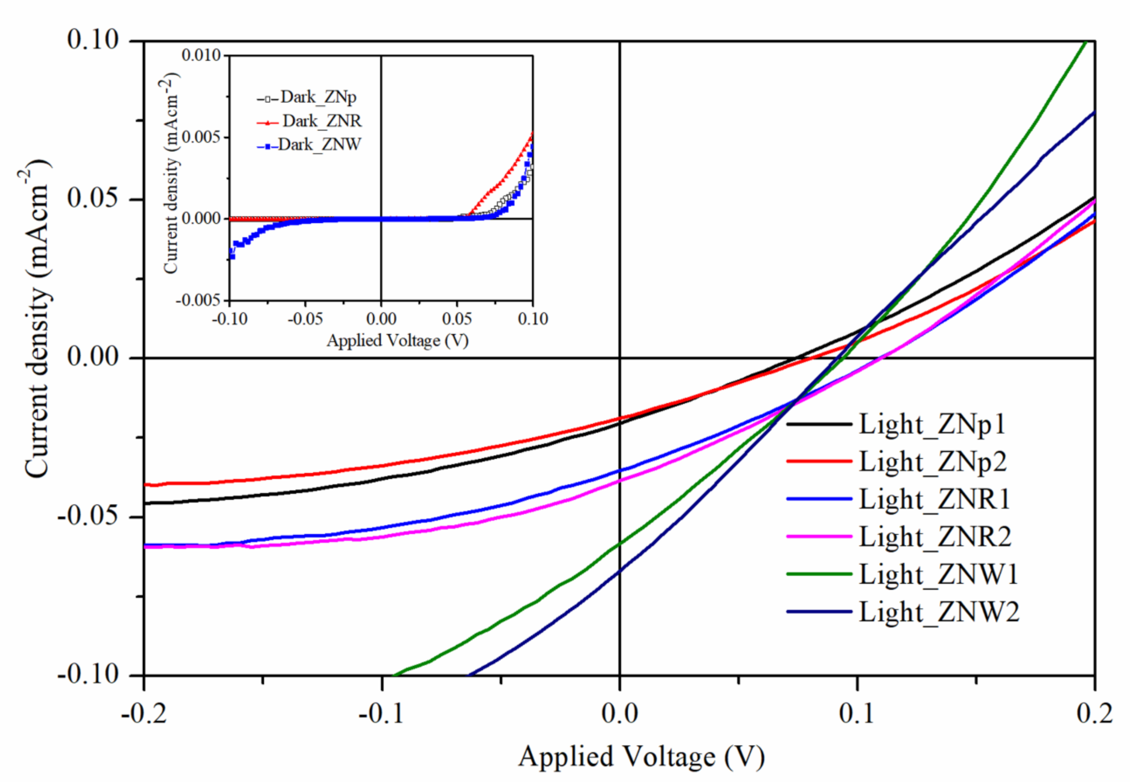

FIGURE 6.36 J-V characteristics of KNBNN based Ag/MoO_3/KNBNN/ZnONS/FTO heterojunction in dark and light illumination. The Inset shows the dark J-V curve for devices with the ZnO nanoparticles, nanorods and nanowalls.

Fig. 6.37 illustrates the energy profiles of the n-i-p devices. The energy levels in Ag/MoO_3/KNBNN/ZnONS/FTO junction are perfectly matched for charge separation. The energy levels for ZnO nanostructures are in the range of 4.2-4.3 eV. FTO has energy level 4.7 eV and Ag has 4.5 eV, that are suitable for charge transportation in device. Thin MoO_3 layer is inserted before Ag electrode as it has suitable energy levels and act as a barrier between anode and intrinsic layer and blocks the electrons before reaching at anode. The suitable energy offset between FTO and ZnO nano structures is beneficial for the enhancement of open circuit voltage of devices.

Fig 6.38 presents the schematic 3-D model of energy level diagram for MoO_3/KNBNN/ZnO-Nanorods hetrojunction showing the internal photo-electric process. The conduction band of ZnO nanorods is lower than the conduction band of photoactive layer KNBNN, which help to transport the photoexcited electrons from KNBNN to FTO electrode. Similar concept was also used by Park et al to explain the photovoltaic behavior [N.-G Park et al. (2013)]. ZnO nanowalls based devices also possess similar internal photoelectric steps as shown in Fig. 6.39. As observed from schematic 3-D model of energy level diagram, the nanowalls provide more junctions for charge separation and transportation, which is another factor for better photocurrent in these devices. Thus, the ZnO nanowalls array are more ideal for light trapping than the ZnO nanorods and nanoparticles implying that the ZnO nanowalls/KNBNN heterostructure can absorb more light because of the arc shaped structure of nanowalls. Because of lowest reflectance from nanowalls, the number of photons near interface speed up the charge separation process inside device and due to nanosized walls the charge carrier transportation is increased.

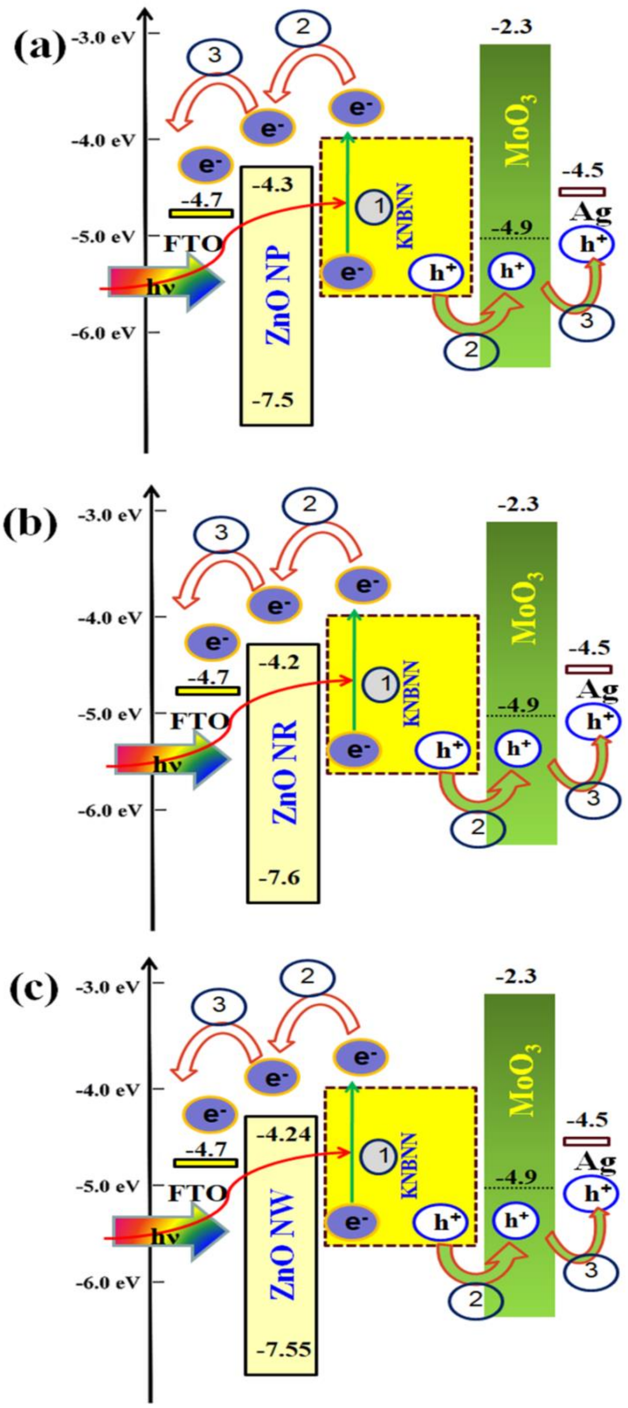

FIGURE 6.37 A schematic representation illustrating energy level diagram for multi- junction device showing the internal photo-electric process.

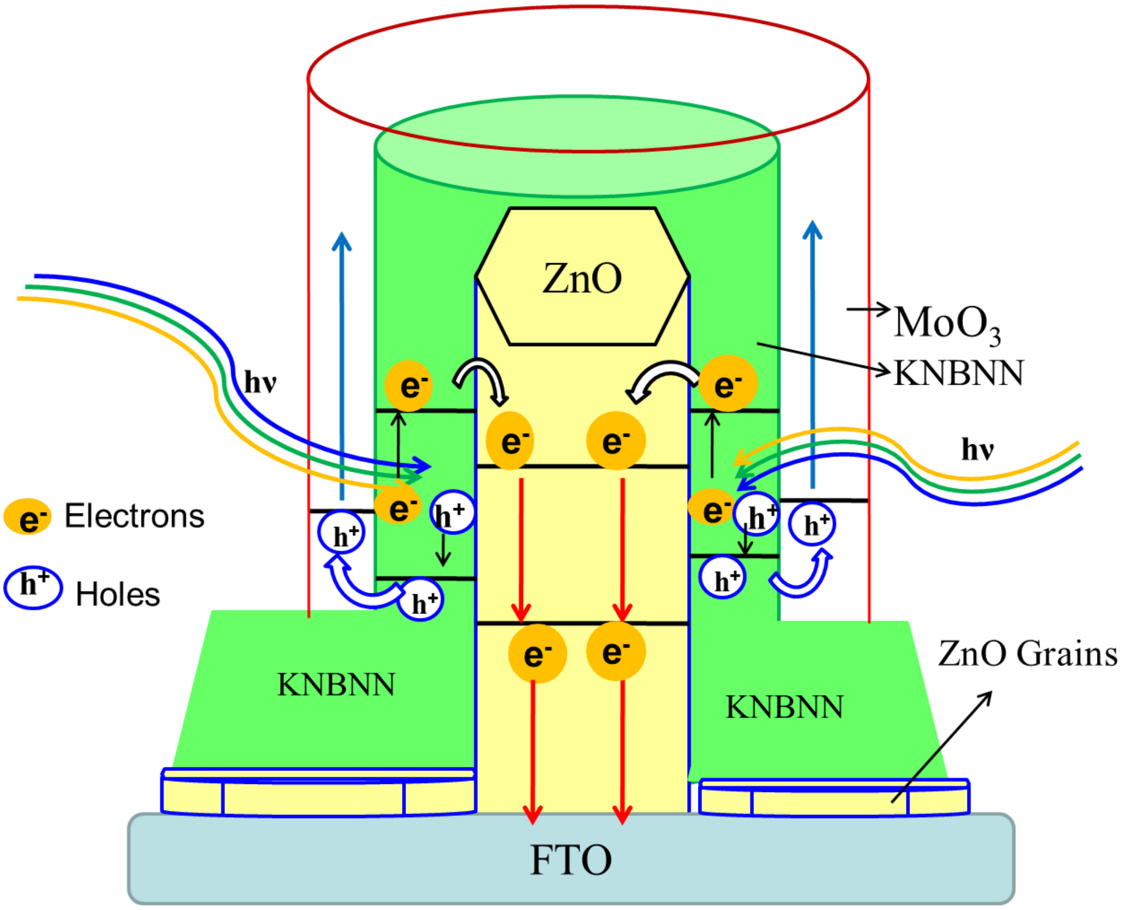

FIGURE 6.38 Schematic energy level diagram for MoO_3/KNBNN/ZnO-Nanorods hetrojunction showing the internal photo-electric process.

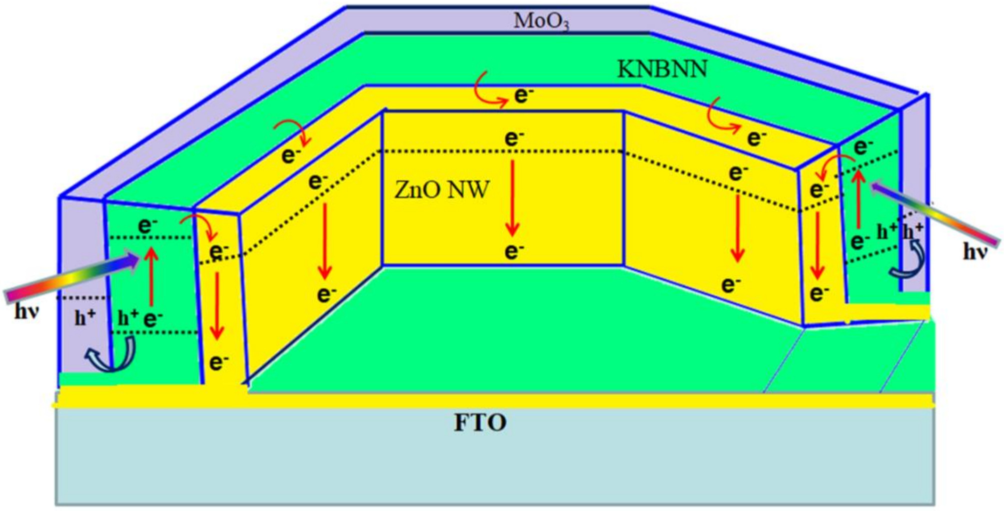

FIGURE 6.39 Schematic energy level diagram for MoO_3/KNBNN/ZnO-Nanowalls hetrojunction showing the internal photo-electric process.

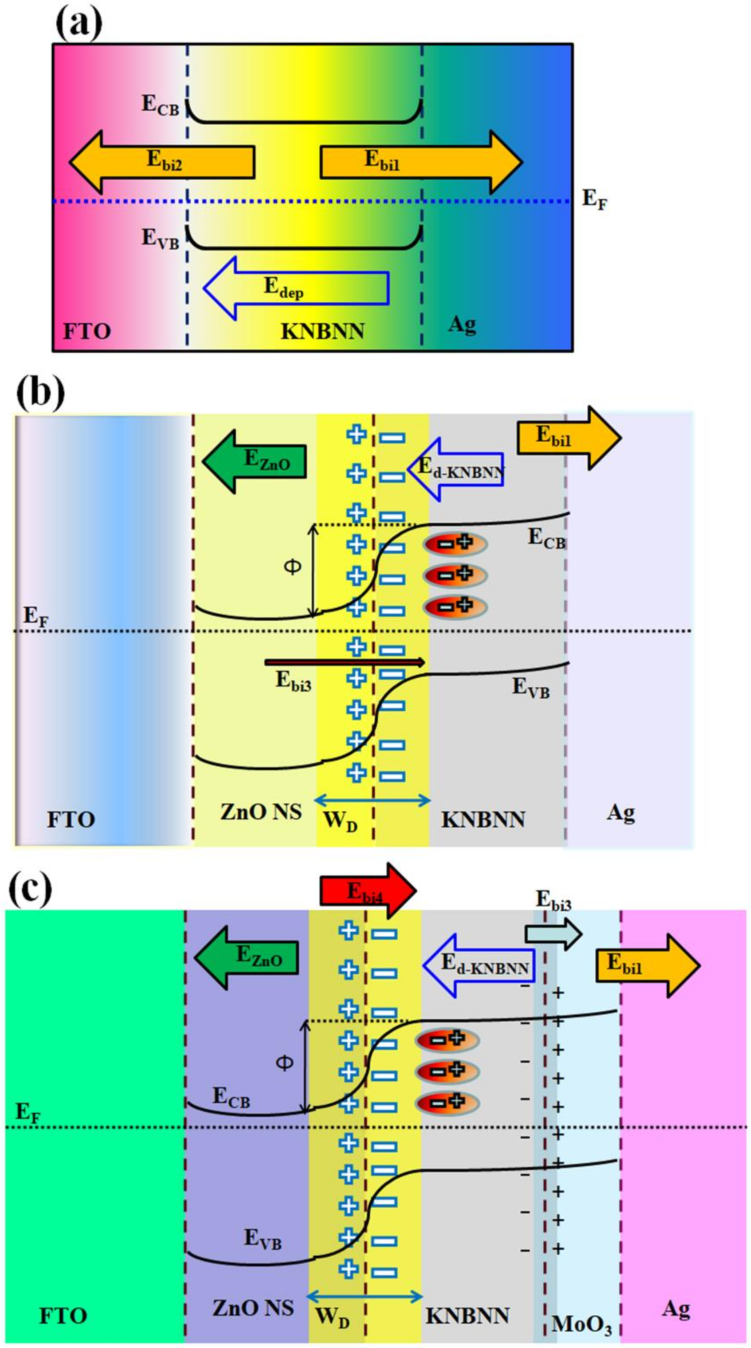

FIGURE 6.40 Illustration of the schematic energy level diagram for (a) Ag/KNBNN/FTO (b) Ag/KNBNN/ZnO NS/FTO (c) Ag/MoO_3/KNBNN/ZnO NS/FTO multi- junction showing the internal photo-electric process.

To further elucidate photovoltaic response in Ag/KNBNN/ZnONS/FTO device, we have analyzed the possible built-in-field (E_{bi}) at interface of layers and depolarization field (E_{dp}) within KNBNN layer. The schematic energy band diagram showing the distribution of built-in-field, depolarization field and possible photovoltaic mechanism of devices is shown in Fig 6.40 (a) Ag/KNBNN/FTO (b) Ag/KNBNN/ZnO NS/FTO (c) Ag/MoO_3/KNBNN/ZnO NS/FTO. The driving forces that separate electrons and holes to the two electrodes are termed as depolarization field (E_{dep}) and built-in-field (E_{bi}) for single junction Ag/KNBNN/FTO devices. The total internal field in ferroelectric capacitor can be written as $E= E_{bi}+E_{dep}$ [A. B. Swain et al (2019). Built-in-field formed at KNBNN/Ag and KNBNN/FTO interface is termed as E_{bi1} and E_{bi2}. The depolarization field for KNBNN is termed as $E_{d\text{-}KNBNN}$ as shown in Fig. 6.40 (b) & (c). ETL ZnO at KNBNN interface produces an electric field termed as E_{bi4} and near HTL MoO_3/KNBNN interface another electric field E_{bi3} is created with the same direction of E_{bi1}. In the direction of depolarization field of KNBNN ($E_{d\text{-}KNBNN}$), ZnO nanostructure also produces a small electric filed (E_{ZnO}) due to its spontaneous polarization. These electric fields provide direction to photo-carriers and influence the current flow. Enhancement in current can be attributed to extra movement provided to photo-electrons by ETL.

7. CONCLUSIONS

To summarize, in this work the ceramic solid solutions of (1-x)$KNbO_3$-x$Ba(Ni_{1/2}Nb_{1/2})O_3$ (KNBNN) were synthesized by solid state reaction method and their optical properties are presented. The UV-visible absorption spectra of KNBNN reveal that the band gap of KNBNN samples shrinkage from 3.1 eV to 2.1 eV. Here, we report the growth of 0.9KNBNN thin films on FTO coated glass substrates using RF magnetron sputtering. A low short circuit photo-current density of 0.026 mA/cm^2 is obtained for Au/KNBN/FTO devices after poling which increased for Ag/KNBN/FTO devices. The sol-gel based 0.9KNBNN thin films also exhibit photovoltaic behaviour after poling and light trapping ZnO nanostructures layer is employed to further improve the photocurrent in these devices. We have studied the growth of ZnO nanostructures on glass and FTO substrates and their anti-reflective properties. The AFM analysis indicated that larger structure size, rougher surface and low density of interconnected ZnO nanowalls make them a better candidate for light harvesting in solar cells. These findings are not only beneficial to study the growth mechanism of ZnO nanostructures but also provide the evidence that optimal geometry of ZnO nanostructures is highly effective in improving the efficiency of solar cells. The results presented here can provide a guideline to develop light trapping methodology needed to achieve higher efficiencies in solar cells. Certainly, the nanostructured materials will have a great promise in future for architecting interface of heterostructure in electronic devices and our results further open a new possibility for promising application of ferroelectric oxide materials in optoelectronic devices.